



Modelling moving contact lines on inextensible elastic sheets in two dimensions

Jin Yao¹, Zhen Zhang² and Weiqing Ren^{1,†}

¹Department of Mathematics, National University of Singapore, Singapore 119076

²Department of Mathematics, Guangdong Provincial Key Laboratory of Computational Science and Material Design, SUSTech International Center for Mathematics, National Center for Applied Mathematics (Shenzhen), Southern University of Science and Technology, Shenzhen, Guangdong 518055, PR China

(Received 6 June 2022; revised 14 December 2022; accepted 15 December 2022)

Elastocapillarity has attracted increasing interest in recent years due to its important roles in many industrial applications. In this work, we derive a thermodynamically consistent continuum model for the dynamics of two immiscible fluids on a thin and inextensible elastic sheet in two dimensions. With the sheet being modelled by a deformable curve with the Wilmore energy and local inextensibility constraint, we derive a two-phase hydrodynamics model with the interfacial and boundary conditions consistent with the second law of thermodynamics. In particular, the boundary conditions on the sheet and at the moving contact line take the form of force balances involving the fluid stress, surface tensions, the sheet bending force and sheet tension, as well as friction forces arising from the slip of fluids on the sheet. The resulting model obeys an energy dissipation law. To demonstrate its capability of modelling complex elastocapillary interactions, we consider two applications: (1) the relaxation dynamics of a droplet on an elastic sheet and (2) the transport of a droplet driven by bendotaxis in a channel bounded by elastic sheets. Numerical solutions for the coupled fluid–sheet dynamics are obtained using the finite element method. The detailed information provided by the full hydrodynamics model allows us to better understand the dynamical processes as compared to other simplified models that were used in previous work.

Key words: contact lines, membranes, multiphase flow

1. Introduction

Elastocapillarity involving the interplay of capillary and elastic forces has received much attention in recent years (Style *et al.* 2017; Bico, Reyssat & Roman 2018; Andreotti &

† Email address for correspondence: matrw@nus.edu.sg

Snoeijer 2020). This is due to the fact that elastocapillary phenomena are common in our everyday life, e.g. the clumping of wet hair or paintbrush bristles, the buckling of pulmonary airways, etc. Elastocapillarity is also relevant to many industrial applications at the microscopic scale. For example, in microelectromechanical systems (MEMS), it is known that elastocapillary interactions are responsible for the collapse of microstructures in humid environments. This leads to an irreversible system failure and poses major fabrication difficulties in MEMS.

There has been much work on elastocapillary problems involving elastic slabs. Consider a liquid drop deposited on an elastic substrate for example. Interesting phenomena occur at the contact line where the fluid interface meets the solid surface. For example, the substrate can be deformed by the capillary force of the drop, resulting in a wetting ridge (Shanahan 1987*b*; Carré, Gastel & Shanahan 1996; Pericet-Cámara *et al.* 2008; Das *et al.* 2011; Jerison *et al.* 2011; Limat 2012; Style *et al.* 2013; Hui & Jagota 2014; Pozrikidis & Hill 2014; Bardall, Daniels & Shearer 2018); the contact angle of the fluid interface may violate the classical Young–Dupré equation (Shanahan 1987*b*; Style & Dufresne 2012; Style *et al.* 2013). The deformation of the substrate also affects the contact line dynamics (Shanahan 1988; Carré *et al.* 1996; Extrand & Kumagai 1996; Kajiya *et al.* 2013; Karpitschka *et al.* 2015; Howland *et al.* 2016).

When the substrate is thin, its deformation is roughly uniform across the thickness thus it can be effectively modelled by a two-dimensional (2-D) elastic sheet with bending and stretching energies. The bending of such an elastic sheet by capillary forces occurs on the length scale $l_B = \sqrt{Et^3/24(1-\nu^2)\gamma}$, where γ is the fluid surface tension, and E , ν and t are the Young's modulus, the Poisson ratio and the thickness of the substrate, respectively (Bico *et al.* 2018). Bending of elastic sheets leads to an enhancement of capillary rise (Kim & Mahadevan 2006). It also enables elastic sheets to spontaneously wrap liquid droplets, a process called capillary origami in the literature. Py *et al.* (2007, 2009) derived a folding criterion in terms of the size of the sheet from the balance of elastic and capillary effects. They also showed that folded structures can be controlled by tailoring the initial sheet geometry. Antkowiak *et al.* (2011) showed the folding process was accelerated using drop impact, and different three-dimensional (3-D) structures were produced from a given sheet by varying the impact speed and the location of impact. Folding of an elastic sheet around a deposited drop was studied by Neukirch, Antkowiak & Marigo (2013) using a variational approach. Brubaker & Lega (2016) derived equilibrium equations for folded origami systems with pinned contact lines by minimizing the sum of the interfacial and elastic energies; the work was later extended to the case of a partial wetting droplet on inextensible elastic sheets in two dimensions (Brubaker 2019). The folded structure was also investigated based on governing equations obtained from mechanical equilibrium (Péraud & Lauga 2014). When the sheet is ultra-thin with negligible bending energy, the final shape of the folded structure is determined by geometric constraints which only involve interfacial energies (Paulsen *et al.* 2015). On an ultra-thin elastic sheet, the capillary force from a deposited drop can induce wrinkles. The size of the wrinkled region, the pattern of wrinkling as well as its mechanism have been studied in many work, e.g. Huang *et al.* (2007), Vella, Adda-Bedia & Cerda (2010), Schroll *et al.* (2013) and Davidovitch & Vella (2018).

In contrast to the large body of work on static problems involving thin sheets, there have been very few studies concerning the dynamics. Duprat, Aristoff & Stone (2011) studied the dynamics of the rise of a wetting liquid between flexible sheets. Bradley *et al.* (2019); Bradley, Hewitt & Vella (2021) and Zhang & Qian (2022) investigated the spontaneous movement of a liquid droplet in a thin channel formed by elastic sheets, a

process called bendotaxis. Taroni & Vella (2012) developed a dynamic model to study the elastocapillary interaction of a liquid drop with the bounding elastic beams and investigated equilibrium configurations of the system as the steady limit of the dynamics. The model took into account the effects of both the Laplace pressure in the bulk of the droplet and the line force at the contact line on the deflection of the beams. All these works were based on the lubrication approximation for the fluid dynamics. Antkowiak *et al.* (2011) developed a 2-D model for the folding dynamics of elastic sheets induced by drop impact. There, after the initial spreading of the drop, the fluid dynamics was assumed to relax sufficiently fast so that the drop was in quasi-static state with the contact lines pinned and separated by a prescribed distance. Only the dynamics of the elastic sheets was considered in their model. Nevertheless, good agreements of the dynamics and the final shape of the sheet with experiments were obtained.

Aside from the above theoretical work, effective numerical methods were also proposed to simulate the dynamics. For example, Alben *et al.* (2019) developed semi-implicit numerical methods to approximate the over-damped dynamics of elastic sheets. The numerical methods have a better stability property as compared to explicit discretization methods, thus allow larger time steps. Barrett, Garcke & Nürnberg (2017, 2020) developed parametric finite element methods to simulate surface evolutions, e.g. the dynamics of biomembranes with the Willmore energy (Helfrich 1973). Numerical methods were also developed for systems involving moving contact lines, e.g. Wouters *et al.* (2019), Pepona *et al.* (2021) and Chen & Zhang (2022). These methods use the lattice Boltzmann method or dissipative particle dynamics to model the fluid dynamics and various discrete models for the elastic sheet. The coupling of the fluids and the sheet is usually achieved through interactions between the fluid and solid particles.

In the current work, we focus on the dynamics of elastocapillarity. Specifically, we derive a thermodynamically consistent model for the dynamics of two immiscible fluids or two phases of one fluid on a thin and inextensible elastic sheet in two dimensions. The fluid dynamics is modelled by the Stokes equations. The elastic sheet is characterized by the Willmore bending energy and a local inextensibility constraint. This type of elastic sheet is widely used in modelling vesicles (Kusumaatmaja *et al.* 2009; Kusumaatmaja & Lipowsky 2011; Zhao, Spann & Shaqfeh 2011; Yazdani & Bagchi 2012; Zhao & Shaqfeh 2013; Farutin & Misbah 2014; Luo & Bai 2015). The total energy of the system consists of the interfacial and bending energies. We follow principles of non-equilibrium thermodynamics to derive the simplest interfacial and boundary conditions. We obtain these conditions from the consideration of the energy dissipation of the dynamical system. Specifically, we identify the relevant fluxes and their corresponding forces in the energy dissipation, then we connect these fluxes and their corresponding forces using constitutive relations, e.g. linear functions as the simplest one. This energy-based framework is rather general and standard. It has been used in earlier works, for example, to derive boundary conditions at the moving contact line on rigid solid substrates (Ren, Hu & Weinan 2010; Ren & Weinan 2011) and for the moving contact line problem involving soluble surfactants (Zhao, Ren & Zhang 2021). For the current problem, the derived model consists of the Stokes equations for the fluid dynamics, the standard conditions on the fluid interface, the kinematic and inextensibility conditions of the sheet as well as the boundary conditions on the sheet and at the moving contact line. These boundary conditions can be phrased as the balance of various forces.

- (i) In the tangential direction of the sheet, the fluid shear stress, the friction force and the gradient of the sheet tension balance each other (see (3.17*a*) and (3.18)). In the

normal direction of the sheet, the fluid normal stress is balanced by the forces arising from the surface and bending energies (see (3.17*b*)).

- (ii) At the moving contact line, the Young stress arising from the deviation of the contact angle from the equilibrium Young's angle, the friction force and the jump of the sheet tension balance each other in the sheet's tangential direction (see (3.22*b*) and (3.23)). The tension of the fluid interface balances the jump of the curvature gradient of the sheet in the normal direction (see (3.22*a*)).

In this model, the energy of the system is dissipated through three channels: the viscous force in the bulk of the fluids, the friction at the fluid–sheet interface and the friction at the moving contact line.

Using this model, we simulate the relaxation dynamics of a droplet on an elastic sheet and the droplet transport driven by bendotaxis. Bendotaxis is a mechanism for droplet self-transport in a thin channel formed by two deformable sheets. The sheets are fixed at one end of the channel and free to move at the other end. A droplet confined in the channel moves simultaneously towards the free end as a result of the interaction of the elastic and capillary forces. Understanding the transport dynamics is important for industrial applications, e.g. in designing self-cleaning surfaces. In this work, we employ the derived model to investigate the mechanism of bendotaxis as well as the effects of the droplet wettability and the sheet stiffness on the dynamics. The numerical method in both applications is a finite element method based on a weak formulation of the model. The method is an extension of the parametric finite element method (Barrett *et al.* 2020) to problems involving moving contact lines.

The rest of the paper is organized as follows. In § 2, we consider the static problem. We first introduce the energy then review the governing equations for the equilibrium system. In § 3, we consider the dynamical problem. We derive the boundary conditions on the elastic sheet and at the moving contact line from the consideration of thermodynamics. Sections 4 and 5 are devoted to applications. We use the derived model to simulate the relaxation dynamics of a droplet on an elastic sheet in § 4 and the droplet motion driven by bendotaxis in § 5. The paper is concluded in § 6.

2. Energetics

We consider the system of two immiscible fluids (fluid 1 and fluid 2) in contact with an elastic sheet in the two-dimensional space, as shown in figure 1. The two fluid regions are denoted by Ω_1 and Ω_2 , respectively. The sheets in contact with fluid 1 and fluid 2 are denoted by Σ_1 and Σ_2 , respectively. The whole sheet $\Sigma_1 \cup \Sigma_2$ is denoted by \mathcal{E} . The contact lines are denoted by Λ . Furthermore, we denote the unit tangent vector to Σ_i ($i = 1, 2$) by $\boldsymbol{\tau}$. The unit normal vector to Σ_i ($i = 1, 2, 3$) is denoted by \boldsymbol{n} , where \boldsymbol{n} points away from the fluid region on the sheet and from Ω_1 to Ω_2 on the fluid–fluid interface. The curvature κ of Σ_i is defined as

$$\kappa = \begin{cases} \nabla_s \cdot \boldsymbol{n}, & \text{on } \Sigma_1, \Sigma_2, \\ -\nabla_s \cdot \boldsymbol{n}, & \text{on } \Sigma_3, \end{cases} \quad (2.1)$$

where ∇_s is the surface gradient operator and the negative sign is due to the fact that \boldsymbol{n} points upwards on Σ_3 . Furthermore, let \boldsymbol{m}_i be the unit conormal vector of Σ_i ($i = 1, 2, 3$) at the contact line, as shown in figure 1(*b*).

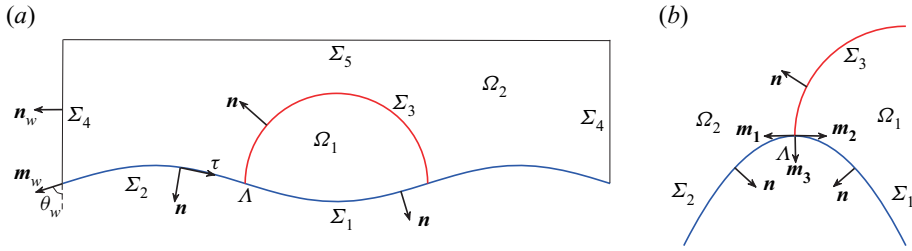


Figure 1. (a) A droplet on an elastic sheet confined in a box. (b) The three interfaces near the contact line.

The total free energy of the system is given by

$$\mathcal{E} = \sum_{i=1}^3 \gamma_i |\Sigma_i| + \frac{c_b}{2} \int_{\mathcal{E}} \kappa^2 ds, \quad (2.2)$$

where the first term models the interfacial energy and the second term, known as the Willmore energy, models the bending energy of the sheet. Here, γ_i ($i = 1, 2, 3$) are the interfacial tension coefficients of the fluid–sheet and fluid–fluid interfaces, $|\Gamma_i|$ ($i = 1, 2, 3$) are the arc lengths of the interfaces and c_b is the bending modulus of the sheet.

The static profiles of the fluid–fluid interface and the sheet as well as the contact angle can be obtained by minimizing the above energy under the area conservation constraint. In a related work (Zhang, Yao & Ren 2020), we studied the equilibrium configuration of a droplet on an elastic membrane in two and three dimensions. The 2-D membrane model took the same form as the one considered here in (2.2). In the following, we briefly review the main results regarding the equilibrium equations in 2-D as well as their asymptotic solutions in the limits of large and small bending modulus, respectively. We note that such a variational approach has been used in earlier work and similar equilibrium equations have been derived (Shanahan 1987a; Neukirch *et al.* 2013; Brubaker 2019). For example, under the assumption of radial symmetry, equilibrium equations were derived by variation of the total energy, where the sheet elastic energy was described by the bending energy (Shanahan 1985, 1987a) and the FvK model consisting of both stretching and bending energies (Olives 1993, 1996), respectively. More recently, a variational approach was employed to study equilibrium configurations of capillary folding in two dimensions (Neukirch *et al.* 2013; Brubaker 2019) and in three dimensions using the FvK model with pinned contact line (Brubaker & Lega 2016).

The governing equations for the static configuration of the system read

$$\gamma_i \kappa - c_b \left(\Delta_s \kappa + \frac{1}{2} \kappa^3 \right) - \lambda_i = 0, \quad \text{on } \Sigma_i \ (i = 1, 2), \quad (2.3a)$$

$$-\gamma_3 \kappa + \lambda_2 - \lambda_1 = 0, \quad \text{on } \Sigma_3, \quad (2.3b)$$

$$\llbracket \kappa \rrbracket_2^1 = 0, \quad \gamma_3 \mathbf{m}_3 - (\gamma_2 - \gamma_1) \mathbf{m}_1 + c_b \left(\mathbf{m}_1 \cdot \llbracket \nabla_s \kappa \rrbracket_2^1 \right) \mathbf{n}|_{\mathcal{E}} = \mathbf{0}, \quad \text{at } \Delta, \quad (2.3c)$$

$$\kappa = 0, \quad \gamma_2 \cos \theta_w + c_b (\mathbf{m}_w \cdot \nabla_s \kappa) \sin \theta_w = 0, \quad \text{at } \partial \mathcal{E}, \quad (2.3d)$$

where λ_1 and λ_2 are Lagrange multipliers for the conservation of the area of Ω_1 and Ω_2 , respectively, and $\mathbf{n}|_{\mathcal{E}}$ is the unit normal vector of the sheet at the contact line. The last equation is the natural boundary condition at the boundary of the sheet, where $\theta_w \in [0, \pi]$ is the angle between the downward tangent vector of the wall Σ_4 and the unit conormal

vector \mathbf{m}_w of the sheet, as depicted in figure 1(a). From the contact line condition (2.3c), we see that the Young–Dupré equation $\gamma_3 \cos \theta_Y = \gamma_2 - \gamma_1$ holds in the tangent direction of the sheet with $\theta_Y = \cos^{-1}(\mathbf{m}_3 \cdot \mathbf{m}_1)$ being the Young’s angle. In addition, we have $\gamma_3 \sin \theta_Y = -c_b(\mathbf{m}_1 \cdot \llbracket \nabla_s \kappa \rrbracket_2^1)$ in the normal direction of the sheet, which states that the surface tension force in the normal direction is balanced by the force resulting from the jump of $\nabla_s \kappa$ across the contact line. We note that a sheet with the inextensibility constraint (see (3.6)) satisfies the same equilibrium equations in (2.3), where the constant Lagrange multiplier for the constraint is absorbed into the surface tension.

Asymptotic solutions were obtained for the above system in the limits as c_b tends to $+\infty$ and 0^+ , respectively (Zhang *et al.* 2020). In the stiff limit as $c_b \rightarrow +\infty$, the leading order solution is given by the configuration in which a circular droplet sits on a rigid substrate with the Young’s contact angle. In the soft limit as $c_b \rightarrow 0^+$, the sheet profile exhibits a transition layer in the vicinity of the contact line, and leading-order solutions in the inner (transition) and outer regions were obtained using the matched asymptotic technique. While the real contact angle of the fluid interface still satisfies the Young–Dupré equation, the apparent contact angles obey Neumann’s law,

$$\frac{\sin \theta_{12}}{\gamma_3} = \frac{\sin \theta_{23}}{\gamma_1} = \frac{\sin \theta_{31}}{\gamma_2}, \tag{2.4}$$

where θ_{ij} is the apparent contact angle between the interfaces Σ_i and Σ_j in the outer region.

3. Dynamical theory

Next we turn our attention to the dynamical problem. We parametrize the fluid–fluid interface as $\mathbf{r}(\zeta, t)$ and the sheet as $\mathbf{q}(\xi, t)$, where $\zeta = 0$ and $\xi = \xi_{cl}(t)$ correspond to the (left) contact line

$$\mathbf{r}(\zeta, t)|_{\zeta=0} = \mathbf{q}(\xi, t)|_{\xi=\xi_{cl}(t)}. \tag{3.1}$$

The velocity of the fluid interface and the sheet are given by $\dot{\mathbf{r}} = (\partial/\partial t)\mathbf{r}(\zeta, t)$ and $\dot{\mathbf{q}} = (\partial/\partial t)\mathbf{q}(\xi, t)$, respectively. Differentiation of (3.1) with respect to time gives the following kinematic relation at the contact line

$$\dot{\mathbf{r}} = \dot{\mathbf{q}} + |\partial_\xi \mathbf{q}| \dot{\xi}_{cl} \boldsymbol{\tau}, \tag{3.2}$$

where $|\partial_\xi \mathbf{q}|$ is the magnitude of the vector $(\partial/\partial \xi)\mathbf{q}(\xi, t)$ and $\dot{\xi}_{cl} = (d/dt)\xi_{cl}(t)$ is the velocity of the contact line in the reference domain. We assume that the following continuity conditions hold at the contact line

$$\llbracket \mathbf{q} \rrbracket_2^1 = \mathbf{0}, \quad \llbracket \partial_\xi \mathbf{q} \rrbracket_2^1 = \mathbf{0}, \tag{3.3a,b}$$

where $\llbracket \cdot \rrbracket_2^1$ denotes the jump across the contact line from Σ_2 to Σ_1 . These conditions imply that $\mathbf{m}_2 = -\mathbf{m}_1$ at the contact line. The same equations hold at the right contact line depicted in figure 1(a).

We assume that the two fluids are simple incompressible fluids, and their dynamics are governed by the time-independent Stokes equations

$$-\nabla p + \nabla \cdot \boldsymbol{\sigma}_i = \mathbf{0}, \tag{3.4a}$$

$$\nabla \cdot \mathbf{u} = 0, \tag{3.4b}$$

in Ω_i ($i = 1, 2$). Here, \mathbf{u} is the fluid velocity, p is the pressure, $\boldsymbol{\sigma}_i = \eta_i(\nabla \mathbf{u} + (\nabla \mathbf{u})^T)$ is the viscous stress, and η_i is the viscosity of fluid i .

As usual, we assume that the fluid velocity is continuous across the fluid–fluid interface and this interface is advected by the fluid velocity

$$[[\mathbf{u}]]_2^1 = \mathbf{0}, \quad \text{on } \Sigma_3, \tag{3.5a}$$

$$\dot{\mathbf{r}} = \mathbf{u}, \quad \text{on } \Sigma_3, \tag{3.5b}$$

where, with a slight abuse of notation, we use $[[\cdot]]_2^1$ to denote the jump across the fluid–fluid interface from fluid 2 to fluid 1 as well.

The sheet is assumed to be locally inextensible and satisfies the inextensibility condition

$$\nabla_s \cdot \dot{\mathbf{q}} = 0. \tag{3.6}$$

Furthermore, the sheet obeys the kinematic condition

$$\dot{\mathbf{q}} \cdot \mathbf{n} = \mathbf{u} \cdot \mathbf{n}, \quad \text{on } \mathcal{E}, \tag{3.7}$$

which is also the non-penetration condition for the fluids.

To close the system, we need additional conditions on the fluid–fluid interface and the sheet and at the moving contact line. Conditions at the outer (left, right and top) boundaries are specific to the problem setup and will be discussed later in the applications. The stress conditions on the fluid–fluid interface are well known, and our main interest here is to derive boundary conditions on the sheet and at the moving contact line. However, it will be more convenient for us to treat the conditions on the fluid–fluid interface and those on the elastic sheet on the same footing.

3.1. Thermodynamics and boundary/interface conditions

We will follow the principles of non-equilibrium thermodynamics to look for the simplest interface and boundary conditions. These conditions are consistent with the second law of thermodynamics, which, in the present context, means that the energy dissipation rate of the system has to be non-positive.

The total energy is given in (2.2). Let us compute the time derivative of each term. Since our main focus here is the boundary conditions on the sheet and at the contact line, we will neglect any possible contribution to the energy dissipation from the outer boundaries.

First of all, for the interfacial energy on $\Sigma_1(t)$, we have

$$\begin{aligned} \frac{d}{dt} \int_{\Sigma_1} \gamma_1 ds &= \int_{\Sigma_1} \gamma_1 (\nabla_s \cdot \dot{\mathbf{q}}) ds + \gamma_1 (|\partial_\xi \mathbf{q}| \dot{\xi}_{cl} (\boldsymbol{\tau} \cdot \mathbf{m}_1)) \Big|_\Lambda, \\ &= \int_{\Sigma_1} \gamma_1 \kappa \dot{\mathbf{q}} \cdot \mathbf{n} ds + \gamma_1 (|\partial_\xi \mathbf{q}| \dot{\xi}_{cl} (\boldsymbol{\tau} \cdot \mathbf{m}_1) + \dot{\mathbf{q}} \cdot \mathbf{m}_1) \Big|_\Lambda \\ &= \int_{\Sigma_1} \gamma_1 \kappa \dot{\mathbf{q}} \cdot \mathbf{n} ds + \gamma_1 (\mathbf{u} \cdot \mathbf{m}_1) \Big|_\Lambda, \end{aligned} \tag{3.8}$$

where $(\cdot)|_\Lambda$ denotes the value at the contact line; in the case of multiple contact lines as in figure 1, it is the sum of the values at all the contact lines. In the last step of the above equation, we have used (3.2) and (3.5b). Similarly, for the interfacial energy on $\Sigma_2(t)$, we have

$$\frac{d}{dt} \int_{\Sigma_2} \gamma_2 ds = \int_{\Sigma_2} \gamma_2 \kappa \dot{\mathbf{q}} \cdot \mathbf{n} ds - \gamma_2 (\mathbf{u} \cdot \mathbf{m}_1) \Big|_\Lambda, \tag{3.9}$$

where we have used the fact that $\mathbf{m}_2 = -\mathbf{m}_1$ at the contact line. For the interfacial energy on $\Sigma_3(t)$, we have

$$\frac{d}{dt} \int_{\Sigma_3} \gamma_3 \, ds = - \int_{\Sigma_3} \gamma_3 \kappa \mathbf{u} \cdot \mathbf{n} \, ds + (\gamma_3 \mathbf{u} \cdot \mathbf{m}_3) \Big|_{\Lambda}, \tag{3.10}$$

where we have used (3.5b).

For the Willmore energy of the sheet, we have

$$\begin{aligned} \frac{d}{dt} \int_{\mathcal{E}} \frac{c_b}{2} \kappa^2 \, ds &= c_b \sum_{i=1}^2 \int_{\Sigma_i} (-\dot{\mathbf{q}} \cdot \mathbf{n}) \left(\Delta_s \kappa + \frac{1}{2} \kappa^3 \right) \, ds \\ &+ c_b \left(-\llbracket \kappa \rrbracket_2^1 \mathbf{m}_1 \cdot \nabla_s (\dot{\mathbf{q}} \cdot \mathbf{n}|_{\mathcal{E}}) + (\mathbf{m}_1 \cdot \llbracket \nabla_s \kappa \rrbracket_2^1) (\dot{\mathbf{q}} \cdot \mathbf{n}|_{\mathcal{E}}) + \frac{1}{2} \llbracket \kappa^2 \rrbracket_2^1 \mathbf{u} \cdot \mathbf{m}_1 \right) \Big|_{\Lambda}, \end{aligned} \tag{3.11}$$

where Δ_s is the Laplace–Beltrami operator. Details for the derivation of this result are provided in [Appendix A](#).

Using the Stokes equation (3.4), we have

$$\begin{aligned} 0 &= \sum_{i=1}^2 \int_{\Omega_i} \mathbf{u} \cdot (\nabla \cdot \mathbf{T}_i) \, dx = - \sum_{i=1}^2 \int_{\Omega_i} \nabla \mathbf{u} : \mathbf{T}_i \, dx + \sum_{i=1}^2 \int_{\partial \Omega_i} \mathbf{n} \cdot \mathbf{T}_i \cdot \mathbf{u} \, ds \\ &= - \sum_{i=1}^2 \int_{\Omega_i} \frac{1}{2\eta_i} \|\sigma_i\|_F^2 \, dx + \sum_{i=1}^2 \int_{\Sigma_i} \mathbf{n} \cdot \mathbf{T}_i \cdot \mathbf{u} \, ds + \int_{\Sigma_3} \mathbf{n} \cdot \llbracket \mathbf{T} \rrbracket_2^1 \cdot \mathbf{u} \, ds, \end{aligned} \tag{3.12}$$

where $\|\cdot\|_F$ denotes the Frobenius norm, $\mathbf{T}_i = -p\mathbf{I} + \sigma_i$, and $\llbracket \mathbf{T} \rrbracket_2^1 = \mathbf{T}_1 - \mathbf{T}_2$.

Corresponding to the local inextensibility condition (3.6), we introduce a Lagrange multiplier ν , named as the tension of the sheet or the sheet tension. Then we have

$$0 = - \sum_{i=1}^2 \int_{\Sigma_i} \nu \nabla_s \cdot \dot{\mathbf{q}} \, ds = \sum_{i=1}^2 \int_{\Sigma_i} [\nabla_s \nu \cdot \dot{\mathbf{q}} - \nu \kappa \dot{\mathbf{q}} \cdot \mathbf{n}] \, ds - (\llbracket \nu \rrbracket_2^1 \dot{\mathbf{q}} \cdot \mathbf{m}_1) \Big|_{\Lambda}. \tag{3.13}$$

Combining (3.8), (3.9), (3.10) and (3.11), and using the identities in (3.12) and (3.13), we obtain

$$\begin{aligned} \frac{d}{dt} \mathcal{E}(t) &= - \sum_{i=1}^2 \int_{\Omega_i} \frac{1}{2\eta_i} \|\sigma_i\|_F^2 \, dx + \int_{\Sigma_3} \left(\llbracket \mathbf{T} \rrbracket_2^1 \cdot \mathbf{n} - \gamma_3 \kappa \mathbf{n} \right) \cdot \mathbf{u} \, ds \\ &+ \sum_{i=1}^2 \int_{\Sigma_i} \left(\mathbf{n} \cdot \mathbf{T}_i + \nabla_s \nu + \left[-c_b \left(\Delta_s \kappa + \frac{1}{2} \kappa^3 \right) + (\gamma_i - \nu) \kappa \right] \mathbf{n} \right) \cdot \dot{\mathbf{q}} \, ds \\ &+ \sum_{i=1}^2 \int_{\Sigma_i} (\mathbf{n} \cdot \mathbf{T}_i \cdot \boldsymbol{\tau})(\mathbf{u} - \dot{\mathbf{q}}) \cdot \boldsymbol{\tau} \, ds \end{aligned}$$

$$\begin{aligned}
 & -c_b \left(\llbracket \kappa \rrbracket_2^1 \mathbf{m}_1 \cdot \nabla_s (\dot{\mathbf{q}} \cdot \mathbf{n}|_{\mathcal{E}}) \right) \Big|_A \\
 & + \left(\left(\llbracket \gamma \rrbracket - \nu + \frac{c_b}{2} \kappa^2 \right) \llbracket \mathbf{m}_1 + \gamma_3 \mathbf{m}_3 + c_b \mathbf{m}_1 \cdot \llbracket \nabla_s \kappa \rrbracket_2^1 \mathbf{n}|_{\mathcal{E}} \right) \cdot \dot{\mathbf{q}} \Big|_A \\
 & + \left(\left(\llbracket \gamma \rrbracket + \frac{c_b}{2} \kappa^2 \right) \llbracket \mathbf{m}_1 + \gamma_3 \mathbf{m}_3 \cdot \mathbf{m}_1 \right) (\mathbf{u} - \dot{\mathbf{q}}) \cdot \mathbf{m}_1 \Big|_A,
 \end{aligned} \tag{3.14}$$

where $\llbracket \gamma \rrbracket_2^1 = \gamma_1 - \gamma_2$. From this equation, we see that the energy dissipation of the system consists of four contributions: the viscous dissipation in the bulk (the first term), the dissipation on the fluid–fluid interface (the second term), the dissipation on the fluid–sheet interface (the third and fourth terms) and the dissipation at the contact line (the last three terms). Each term is in the form of a product of a generalized flux and a generalized force. Next, we examine the implication of this form of energy dissipation for the interface and boundary conditions.

The fluid–fluid interface. In the second term of (3.14), the generalized flux is the fluid velocity \mathbf{u} , and the generalized force is the total force (the viscous stress and the capillary force) acting on the fluid interface. Since the interface is massless, the total force necessarily vanishes according to Newton’s second law. This gives the usual interface condition

$$\llbracket \mathbf{T} \rrbracket_2^1 \cdot \mathbf{n} - \gamma_3 \kappa \mathbf{n} = \mathbf{0}. \tag{3.15}$$

The fluid–sheet interface. In the third term of the energy dissipation in (3.14), the generalized flux is the sheet velocity $\dot{\mathbf{q}}$, the generalized force is the total force acting on the fluid–sheet interface, including the viscous fluid stress, the bending force, the surface tension and the sheet tension. Again, the total force is zero since the interface is massless. This gives

$$\mathbf{n} \cdot \mathbf{T}_i + \nabla_s \nu + \left(-c_b \left(\Delta_s \kappa + \frac{1}{2} \kappa^3 \right) + (\gamma_i - \nu) \kappa \right) \mathbf{n} = \mathbf{0}. \tag{3.16}$$

This is a vector equation, which can be decomposed into the tangential and normal components as

$$\mathbf{n} \cdot \mathbf{T}_i \cdot \boldsymbol{\tau} + \boldsymbol{\tau} \cdot \nabla_s \nu = 0, \tag{3.17a}$$

$$\mathbf{n} \cdot \mathbf{T}_i \cdot \mathbf{n} - c_b \left(\Delta_s \kappa + \frac{1}{2} \kappa^3 \right) + (\gamma_i - \nu) \kappa = 0. \tag{3.17b}$$

These two equations state the force balances in the tangential and normal directions, respectively.

In the fourth term, the generalized flux is the slip velocity of the fluid relative to the sheet, $(\mathbf{u} - \dot{\mathbf{q}}) \cdot \boldsymbol{\tau}$, and the generalized force is the viscous shear stress $\mathbf{n} \cdot \mathbf{T}_i \cdot \boldsymbol{\tau}$. Following the generalized thermodynamics formalism, we relate the generalized force to the generalized flux. We will assume the simplest form for the constitutive relation, namely, the generalized force is a linear function of the generalized flux. This gives us the well-known Navier slip condition

$$\mathbf{n} \cdot \mathbf{T}_i \cdot \boldsymbol{\tau} = -\mu_i (\mathbf{u} - \dot{\mathbf{q}}) \cdot \boldsymbol{\tau}, \tag{3.18}$$

where the right-hand side is the friction force arising from the slip of the fluid on the surface of the sheet with μ_i being the friction coefficient. Equations (3.17a) and (3.18)

show that the viscous shear stress, the friction force and the gradient of the sheet tension balance each other. Thus, the slip condition can be alternatively written as

$$\boldsymbol{\tau} \cdot \nabla_s \mathbf{v} = -\mu_i (\dot{\mathbf{q}} - \mathbf{u}) \cdot \boldsymbol{\tau}. \tag{3.19}$$

The moving contact line. Next we examine the energy dissipation at the contact line given by the last three terms in (3.14). First of all, in the third to last term, the generalized flux is $\mathbf{m}_1 \cdot \nabla_s (\dot{\mathbf{q}} \cdot \mathbf{n}|_{\mathcal{E}})$, which represents the angular velocity of the sheet rotating around the contact line, and the generalized force is given by the jump of the sheet curvature across the contact line. Since the contact line is massless, we set the generalized force to zero. This gives the continuity condition for the sheet curvature at the contact line

$$\llbracket \kappa \rrbracket_2^1 = 0. \tag{3.20}$$

Similarly, from the second to last term, we obtain

$$\llbracket \gamma - \nu \rrbracket_2^1 \mathbf{m}_1 + \gamma_3 \mathbf{m}_3 + c_b \mathbf{m}_1 \cdot \llbracket \nabla_s \kappa \rrbracket_2^1 \mathbf{n}|_{\mathcal{E}} = \mathbf{0}, \tag{3.21}$$

where we have used (3.20). Let θ_d be the dynamic contact angle between the fluid–fluid interface and the sheet, i.e. $\theta_d = \arccos(\mathbf{m}_1 \cdot \mathbf{m}_3)$. Then the above vector equation can be decomposed into the following normal and tangential components as

$$\gamma_3 \sin \theta_d + c_b \mathbf{m}_1 \cdot \llbracket \nabla_s \kappa \rrbracket_2^1 = 0, \tag{3.22a}$$

$$\llbracket \gamma - \nu \rrbracket_2^1 + \gamma_3 \cos \theta_d = 0. \tag{3.22b}$$

These are the force balances at the contact line in the directions normal and tangential to the sheet, respectively. The curvature of the sheet is continuous, as shown in (3.20), but its gradient is discontinuous at the contact line unless $\theta_d = 0$ or π . Equation (3.22a) shows that the jump of the gradient of the sheet curvature balances the surface tension of the fluid–fluid interface in the normal direction, $\gamma_3 \sin \theta_d$. In the tangential direction, as shown in (3.22b), the surface tension of the fluid interface, $\gamma_3 \cos \theta_d$, is balanced by the jump of the effective tension of the sheet, $\llbracket \gamma - \nu \rrbracket_2^1$.

Finally, in the last term of (3.14), the generalized flux is the slip velocity of the contact line, $(\mathbf{u} - \dot{\mathbf{q}}) \cdot \mathbf{m}_1$, and the generalized force is the unbalanced Young stress $\gamma_1 - \gamma_2 + \gamma_3 \cos \theta_d$. We relate these two quantities following the generalized thermodynamics. By assuming a linear relation, we obtain

$$\gamma_1 - \gamma_2 + \gamma_3 \cos \theta_d = -\mu_\Lambda (\mathbf{u} - \dot{\mathbf{q}}) \cdot \mathbf{m}_1, \tag{3.23}$$

where μ_Λ is the friction coefficient at the moving contact line. From (3.22b) and (3.23), we see that the unbalanced Young stress $\gamma_1 - \gamma_2 + \gamma_3 \cos \theta_d$, the friction force $-\mu_\Lambda (\mathbf{u} - \dot{\mathbf{q}}) \cdot \mathbf{m}_1$ and the jump of the sheet tension $\llbracket \nu \rrbracket_2^1$ balance each other at the contact line. Thus, (3.23) can be alternatively written as

$$\llbracket \nu \rrbracket_2^1 = -\mu_\Lambda (\mathbf{u} - \dot{\mathbf{q}}) \cdot \mathbf{m}_1. \tag{3.24}$$

3.2. Dimensionless model and the dissipation law

The Stokes equation (3.4), the conditions (3.5) and (3.15) on the fluid–fluid interface, the conditions (3.6), (3.7), (3.16) and (3.18) on the sheet, the conditions (3.21) and (3.23) at the moving contact line, together with boundary conditions at outer boundaries, form the complete model for the dynamics of the coupled fluids–sheet system.

To make the model dimensionless, we follow the standard practice and rescale \mathbf{x} , \mathbf{r} and \mathbf{q} using the system size L , the fluid velocity \mathbf{u} using the characteristic velocity U , the pressure p using $\eta_1 U/L$, time t using L/U and the total energy \mathcal{E} using $\gamma_3 L$. Furthermore, we rescale the fluid viscosity η_i ($i = 1, 2$) and the friction coefficient μ_Δ using η_1 , the friction coefficient μ_i ($i = 1, 2$) using μ_1 , the surface tension γ_i ($i = 1, 2, 3$) and the sheet tension ν using γ_3 , and the bending modulus c_b using $\gamma_3 L^2$. We define the capillary number Ca and the slip length l_s as

$$Ca = \frac{\eta_1 U}{\gamma_3}, \quad l_s = \frac{\eta_1}{\mu_1 L}. \tag{3.25a,b}$$

Then the dimensionless governing equations are given by

$$\nabla p - \nabla \cdot (\eta_i (\nabla \mathbf{u} + (\nabla \mathbf{u})^T)) = \mathbf{0}, \tag{3.26a}$$

$$\nabla \cdot \mathbf{u} = 0, \tag{3.26b}$$

for the fluids in $\Omega_i(t)$, $i = 1, 2$, together with the following conditions on the fluid interface, on the elastic sheet and at the contact line.

(i) Interface conditions on the fluid interface $\Sigma_3(t)$:

$$\llbracket \mathbf{u} \rrbracket_2^1 = \mathbf{0}, \tag{3.27a}$$

$$Ca \llbracket \boldsymbol{\tau} \rrbracket_2^1 \cdot \mathbf{n} - \kappa \mathbf{n} = \mathbf{0}, \tag{3.27b}$$

$$\dot{\mathbf{r}} = \mathbf{u}. \tag{3.27c}$$

(ii) Conditions on the elastic sheet $\Sigma_i(t)$, $i = 1, 2$:

$$Ca \boldsymbol{\tau}_i \cdot \mathbf{n} + \nabla_s \nu + \left(-c_b \left(\Delta_s \kappa + \frac{1}{2} \kappa^3 \right) + (\gamma_i - \nu) \kappa \right) \mathbf{n} = \mathbf{0}, \tag{3.28a}$$

$$\frac{l_s}{Ca} \nabla_s \nu = -\mu_i (\dot{\mathbf{q}} - \mathbf{u}), \tag{3.28b}$$

$$\nabla_s \cdot \dot{\mathbf{q}} = 0. \tag{3.28c}$$

(iii) Conditions at the moving contact line $\Lambda(t)$:

$$\llbracket \mathbf{q} \rrbracket_2^1 = \llbracket \boldsymbol{\tau} \rrbracket_2^1 = \mathbf{0}, \quad \llbracket \kappa \rrbracket_2^1 = 0, \tag{3.29a}$$

$$\llbracket \gamma - \nu \rrbracket_2^1 \mathbf{m}_1 + \mathbf{m}_3 + c_b \mathbf{m}_1 \cdot \llbracket \nabla_s \kappa \rrbracket_2^1 \mathbf{n}|_\Sigma = \mathbf{0}, \tag{3.29b}$$

$$\frac{1}{Ca} \llbracket \nu \rrbracket_2^1 = -\mu_\Delta (\mathbf{u} - \dot{\mathbf{q}}) \cdot \mathbf{m}_1. \tag{3.29c}$$

Applying these conditions in (3.14), we obtain the following energy dissipation law,

$$\begin{aligned} \frac{d}{dt} \mathcal{E}(t) = & - \sum_{i=1}^2 \int_{\Omega_i(t)} \frac{Ca}{2\eta_i} \|\boldsymbol{\sigma}_i\|_F^2 \, dx \\ & - \frac{Ca}{l_s} \sum_{i=1}^2 \int_{\Sigma_i(t)} \mu_i |\mathbf{u} - \dot{\mathbf{q}}|^2 \, ds - Ca \left(\mu_\Delta |\mathbf{u} - \dot{\mathbf{q}}|^2 \right) \Big|_{\Lambda(t)} \leq 0, \end{aligned} \tag{3.30}$$

where the three terms on the right-hand side represent the rate of energy dissipation in the bulk, on the sheet and at the contact line, respectively.

Equation (3.28*b*) is the governing equation for the dynamics of the material points of the sheet. It can be rewritten as

$$\dot{\mathbf{q}} = \mathbf{u} - \frac{l_s}{\mu_i Ca} \nabla_s v. \tag{3.31}$$

Taking the surface divergence on both sides of the above equation and applying the inextensibility condition (3.28*c*), we obtain

$$\frac{l_s}{\mu_i} \Delta_s v = Ca \nabla_s \cdot \mathbf{u}, \quad \text{on } \Sigma_i(t), \quad i = 1, 2. \tag{3.32}$$

In (3.31), the continuity of $\dot{\mathbf{q}}$ and \mathbf{u} across the contact line implies

$$\left[\left[\frac{1}{\mu_i} \nabla_s v \right] \right]_2^1 = \frac{1}{\mu_1} [\nabla_s v]_1 - \frac{1}{\mu_2} [\nabla_s v]_2 = \mathbf{0}, \tag{3.33}$$

where $[\nabla_s v]_i$ denotes the surface gradient of v at the contact line evaluated on the side of Σ_i ($i = 1, 2$). Furthermore, from (3.29*c*) and (3.31), we obtain the following jump condition for v at the contact line

$$[[v]]_2^1 = -\frac{\mu_\Lambda l_s}{\mu_i} [\nabla_s v]_i \cdot \mathbf{m}_1, \quad i = 1, 2. \tag{3.34}$$

In numerical simulations, it is more convenient to use (3.32) with the jump conditions (3.34) in place of (3.28*c*) to determine the sheet tension v . Once v is known, the configuration of the sheet and its parametrization can be updated according to (3.31). Specifically, the configuration of the sheet can be updated using the normal component of (3.31),

$$\dot{\mathbf{q}} \cdot \mathbf{n} = \mathbf{u} \cdot \mathbf{n}. \tag{3.35}$$

The tangential component of (3.31), i.e.

$$\dot{\mathbf{q}} \cdot \boldsymbol{\tau} = \mathbf{u} \cdot \boldsymbol{\tau} - \frac{l_s}{\mu_i Ca} \boldsymbol{\tau} \cdot \nabla_s v, \tag{3.36}$$

determines the motion of the sheet in the tangential direction, i.e. redistribution of the material points along the sheet, but not its geometry.

3.3. Fluid–vacuum–sheet system

Following the same procedure, we can derive the boundary and interface conditions for a fluid–vacuum–sheet system. Specifically, we consider the situation when fluid 2 in figure 1 is replaced by a vacuum. The fluid dynamics in Ω_1 is still assumed to obey the Stokes equations in (3.4). The fluid–vacuum interface Σ_3 and the fluid–sheet interface Σ_1 obey the kinematic conditions in (3.5*b*) and (3.7), respectively. The sheet and its tangent are continuous at the contact line, so (3.3*a,b*) holds. Then following the generalized thermodynamics formulism as in § 3.1, we can derive the conditions on the sheet and at the moving contact line by analysing the rate of energy dissipation of the system. We skip the details and summarize these (dimensionless) conditions as follows.

- (i) On the fluid–vacuum interface Σ_3 , we have the same conditions as in (3.27), except that the fluid velocity continuity condition (3.27*a*) is not required and the stress jump condition (3.27*b*) is replaced by

$$Ca \mathbf{T}_1 \cdot \mathbf{n} - \kappa \mathbf{n} = \mathbf{0}. \tag{3.37}$$

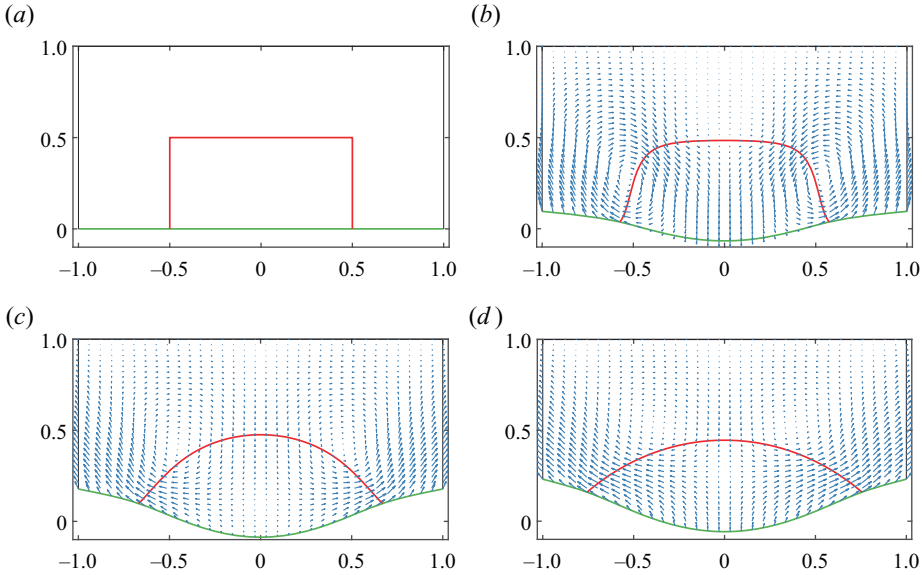


Figure 3. The interface profiles and the fluid velocity for the wetting case ($\theta_Y = \pi/3$): (a) $t = 0$, $\max_{x \in \Omega} |\mathbf{u}| = 0$; (b) $t = 0.05$, $\max_{x \in \Omega} |\mathbf{u}| = 1.207$; (c) $t = 0.2$, $\max_{x \in \Omega} |\mathbf{u}| = 0.478$; (d) $t = 1.0$, $\max_{x \in \Omega} |\mathbf{u}| = 0.027$.

On the left and right boundaries, we use the stress-free condition,

$$\mathbf{T}_2 \cdot \mathbf{n}_w = \mathbf{0}, \tag{4.2}$$

where \mathbf{n}_w is the unit outward normal of the boundary. For the sheet, we use the natural boundary conditions at $x = \pm 1$,

$$v = 0, \tag{4.3a}$$

$$\kappa = 0, \tag{4.3b}$$

$$\gamma_2 \cos \theta_w + c_b (\mathbf{m}_w \cdot \nabla_s \kappa) \sin \theta_w = 0. \tag{4.3c}$$

These conditions allow the material points of the sheet to cross the boundaries at $x = \pm 1$.

Equations (3.26)–(3.29), together with the boundary conditions (4.1)–(4.3), form a complete model for the coupled fluids–sheet system. We simulate the dynamics using the finite element method based on a weak formulation of the model (see Appendix B). We consider two cases: one is a wetting case with $\gamma_1 = 0.5$, $\gamma_2 = 1$ and the equilibrium contact angle $\theta_Y = \pi/3$, the other one is a non-wetting case with $\gamma_1 = 1$, $\gamma_2 = 0.5$ and the equilibrium contact angle $\theta_Y = 2\pi/3$. Other parameters are chosen as $\eta_2 = 0.1$, $\mu_2 = 0.1$, $\mu_A = 0.1$, $Ca = 0.2$, $l_s = 0.1$ and $c_b = 0.1$.

Several snapshots of the system at different times are shown in figure 3 for the wetting case and figure 4 for the non-wetting case. In both cases, the sheet, which is flat initially, is deformed. A pair of vortices in the velocity field form along with the evolution of the fluid interface. In the wetting case, outward velocities are generated at the contact lines driving the droplet to spread on the sheet. In the non-wetting case, the contact lines retreat with inward velocities.

In figure 5(a,b), we show the curvature and in figure 5(c,d) the tension of the elastic sheet at different times. Both the curvature gradient and the tension exhibit a jump across the contact line. The magnitude of the tension decays to 0 as the system approaches

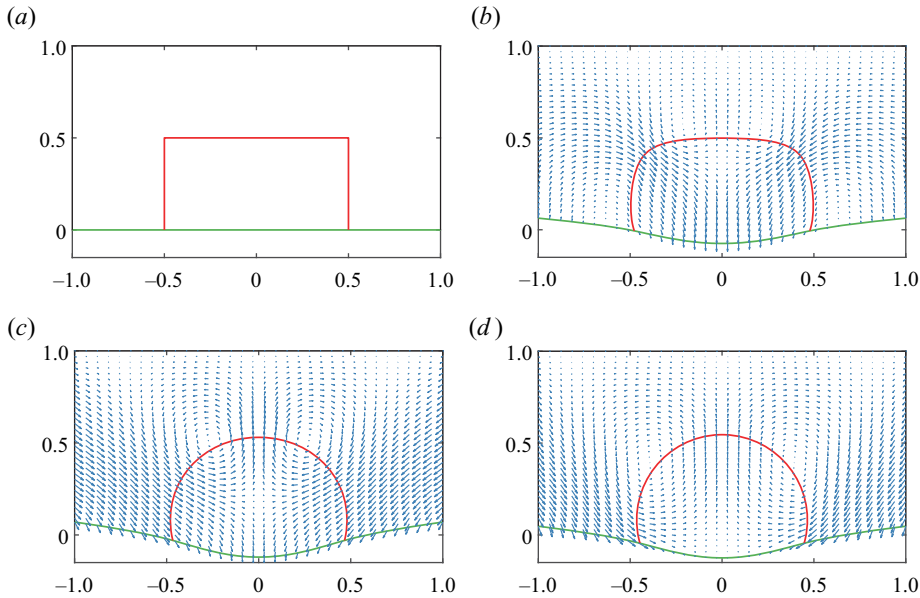


Figure 4. The interface profiles and the fluid velocity for the non-wetting case ($\theta_Y = 2\pi/3$): (a) $t = 0$, $\max_{x \in \Omega} |\mathbf{u}| = 0$; (b) $t = 0.05$, $\max_{x \in \Omega} |\mathbf{u}| = 1.203$; (c) $t = 0.2$, $\max_{x \in \Omega} |\mathbf{u}| = 0.130$; (d) $t = 1.0$, $\max_{x \in \Omega} |\mathbf{u}| = 0.005$.

the equilibrium. The insets of panels (c, d) show the gradient of the tension rescaled by the friction coefficient, $(1/\mu_i)|\nabla_s v|$, along the sheet. We observe that the rescaled gradient is continuous, though the tension itself has a jump at the contact line. Also the rescaled gradient of the tension attains the maximum at the contact line, indicating maximum slip occurs there according to (3.28b).

In figure 6(a), we plot the total energy and in figure 6(b) the bending energy against time. The total energy decays in time, as expected from the energy dissipation property of the dynamical system. The bending energy, however, shows a rapid increase as a result of the deformation of the sheet at an initial stage.

Following the dynamics, the system eventually relaxes to the equilibrium state (steady state). In figure 7, we show the steady-state profiles of the interface and the sheet with large and small bending modulus. In the stiff case ($c_b = 100$), the sheet remains nearly flat and the droplet has the usual shape of a circular arc with the contact angle satisfying the Young–Dupré equation (panels a,c). In the soft case ($c_b = 0.001$), the sheet is significantly deformed (panels b,d). Its curvature undergoes a rapid change near the contact line (the inner region) but is nearly constant away from the contact line (the outer region). The size of the inner region is of the order of $\sqrt{c_b}$. These results agree with the asymptotic solutions discussed in § 2, as shown in panels (c,d), where we overlay the asymptotic solutions in the outer region.

Furthermore, we measured the apparent contact angles formed by the three interfaces in the outer region (see figure 7b). Specifically, we fit the fluid interface using a constant-curvature (circular) arc. The arc goes through the apex of the interface and also fits the curvature of the interface there. Similarly, we fit the sheet under the droplet using a circular arc through the middle point of the sheet. The two arcs intersect at an apparent contact line. The sheet outside the droplet is fitted using a horizontal line through the apparent contact line. The apparent contact angles are then measured between these fitting

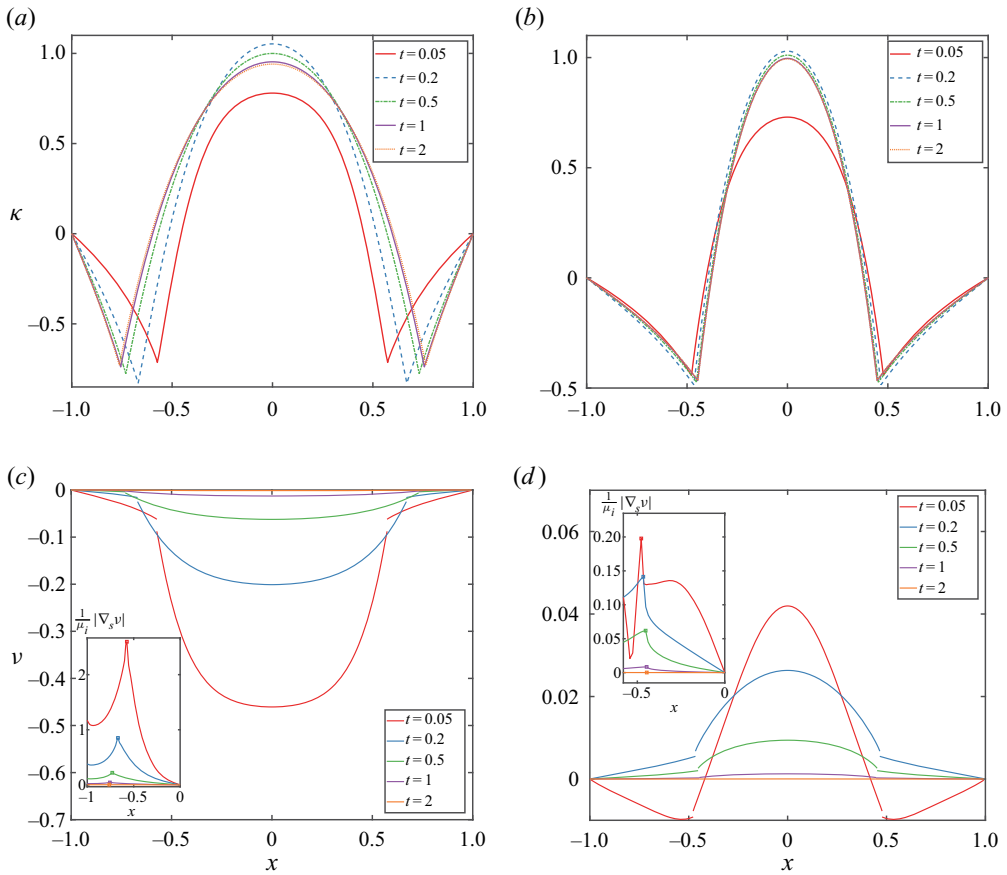


Figure 5. (a,b) Curvature and (c,d) tension of the sheet at different times: (a) curvature, $\theta_Y = \pi/3$; (b) curvature, $\theta_Y = 2\pi/3$; (c) tension, $\theta_Y = \pi/3$; (d) tension, $\theta_Y = 2\pi/3$. The insets in panels (c,d) are plots of $(1/\mu_i)|\nabla_s v|$.

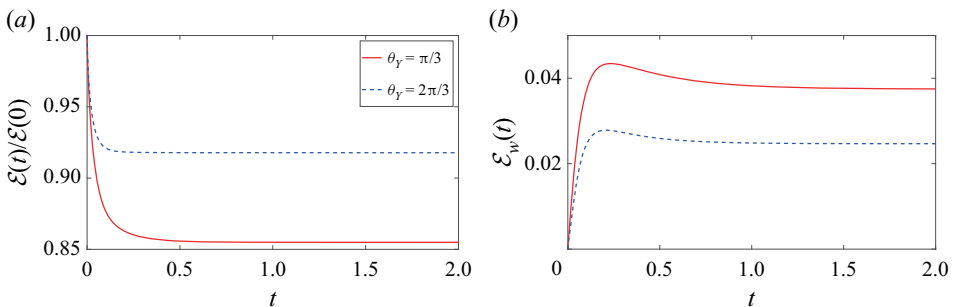


Figure 6. (a) Rescaled energy $\mathcal{E}(t)/\mathcal{E}(0)$ versus time; (b) bending energy, $\mathcal{E}_w(t) = (c_b/2) \int_{\Sigma(t)} \kappa^2 ds$, versus time.

curves at the apparent contact line. The results are reported in [table 1](#) for various small bending modulus. We see that, though the real contact angle satisfies the Young–Dupré equation, the apparent angles converge to the values predicted by Neumann’s law (2.4) as

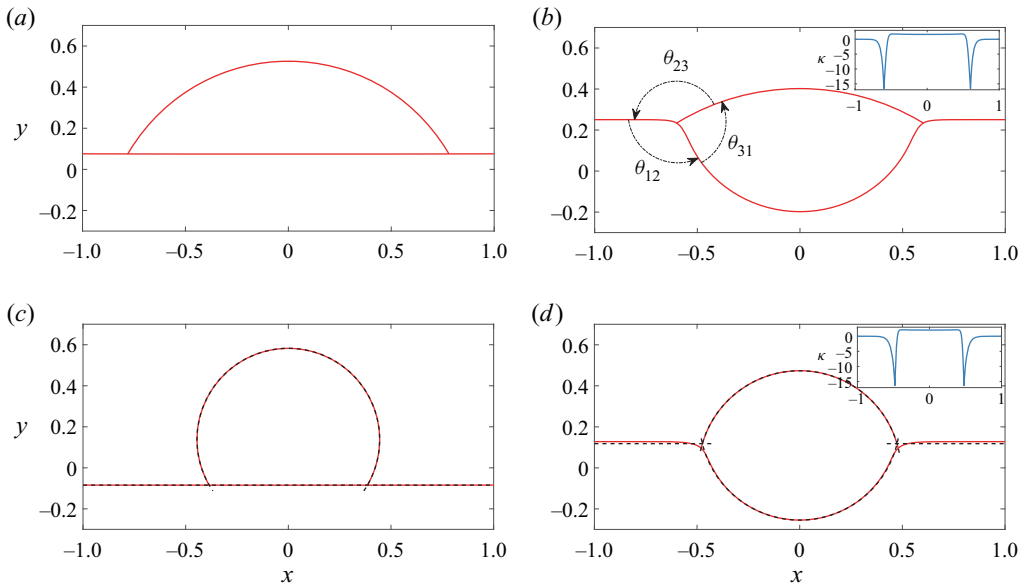


Figure 7. The steady-state profiles of the fluid interface and the sheet: (a) $\theta_Y = \pi/3$, $c_b = 100$; (b) $\theta_Y = \pi/3$, $c_b = 0.001$; (c) $\theta_Y = 2\pi/3$, $c_b = 100$; (d) $\theta_Y = 2\pi/3$, $c_b = 0.001$. The insets in panels (b,d) are plots of the sheet curvature κ . The overlaid black dashed curves in panels (c,d) are plots of the asymptotic solutions in the stiff (panel c) and soft (panel d) limits.

c_b	θ_{12}	θ_{23}	θ_{31}	c_b	θ_{12}	θ_{23}	θ_{31}
0.004	2.0025	2.5733	1.7073	0.004	2.0365	1.7062	2.5405
0.002	1.9493	2.5911	1.7427	0.002	1.9562	1.7578	2.5692
0.001	1.8967	2.6038	1.7827	0.001	1.8826	1.8106	2.5900
0	1.8235	2.6362	1.8235	0	1.8235	1.8235	2.6362

Table 1. The apparent contact angles formed by the three interfaces at the steady state (see figure 7b) for the wetting case (first four columns) and non-wetting case (second four columns). The last row ($c_b = 0$) shows the theoretical values predicted by Neumann’s law (2.4).

the bending modules decrease towards 0. This agrees with the asymptotic results in Zhang *et al.* (2020).

5. Application: bendotaxis

In this application, we consider the dynamics of a droplet driven by bendotaxis. The setup of the system is shown in figure 8. A droplet is confined between two semi-infinite elastic sheets in two dimensions. The left ends of the sheets are fixed at $(0, \pm B_y)$. An interesting phenomenon observed in experiments is that the droplet migrates spontaneously along the channel from the fixed end to the free end (left to right), regardless of the wetting property of the droplet (Bradley *et al.* 2019). Here, we use the model derived in § 3 to simulate the coupled dynamics of the sheets and the droplet.

The droplet is formed by a Newtonian fluid and outside of the droplet is a vacuum. The dynamics is governed by the equations in § 3.3. At the left end $x = 0$ where the sheets are

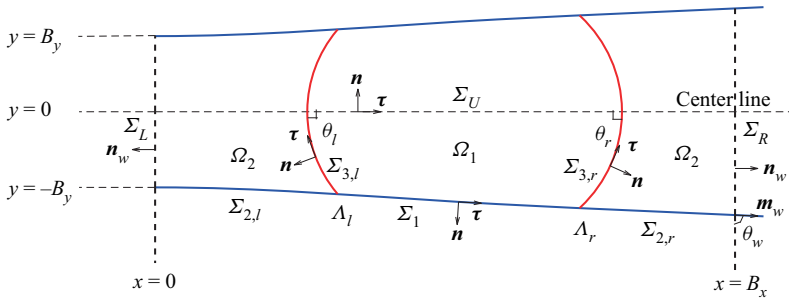


Figure 8. Setup of bendotaxis. A liquid droplet is placed in a channel bounded by two semi-infinite elastic sheets. The left ends of the sheets are fixed at $(0, \pm B_y)$.

fixed, we impose the clamped boundary conditions

$$\dot{\mathbf{q}} = 0, \quad \frac{\partial y}{\partial \xi} = 0, \quad (5.1a,b)$$

where $\mathbf{q}(\xi, t) = (x, y)$. For convenience of the simulation, we use x to parametrize the sheets, $\mathbf{q} = (x, y(x, t))$. We truncate the system on the right at $x = B_x$ and impose the natural boundary conditions for the sheets as given in (4.3). These conditions allow material points of the sheets to cross the boundary at $x = B_x$, thus, although the sheets are inextensible, their lengths over the domain $[0, B_x]$ are not fixed. Furthermore, since the system is symmetric about the centreline of the channel at $y = 0$, we only carry out the computation in the lower half of the channel and impose the symmetry conditions along $y = 0$,

$$\frac{\partial u_1}{\partial y} = 0, \quad u_2 = 0, \quad (5.2a)$$

$$\theta_l = \theta_r = \frac{\pi}{2}, \quad (5.2b)$$

where $\mathbf{u} = (u_1, u_2)$ is the fluid velocity, and θ_l and θ_r are the angles between the fluid–vacuum interfaces and the centreline $y = 0$.

Given an initial configuration of the system, we compute the dynamics by solving the governing equations in § 3.3 together with the boundary conditions (5.1a,b) and (5.2) using the finite element method. Specifically, we compute the fluid velocity, the fluid pressure, the profile of the sheet and its tension, as well as the fluid–vacuum interfaces. Below, we present the numerical results and investigate the mechanism of bendotaxis. We also study the effects of the wettability and bending modulus of the sheets on the dynamics. In all simulations, the initial configuration of the system is prepared by holding the sheets straight while letting the droplet relax until reaching equilibrium with the sheets. Then we release the sheets (except their fixed left ends) and let the system evolve. The contact lines of the initial relaxed droplet are located at $x_l = 2$ and $x_r = 6$, respectively. Other parameters are chosen as $B_x = 10$, $B_y = 0.5$, $\mu_\Lambda = 0.1$, $l_s = 0.1$, $Ca = 0.1$.

We first report numerical results for a wetting case with $\gamma_1 = 0.3$, $\gamma_2 = 1$, $\cos \theta_Y = 0.7$ and a non-wetting case with $\gamma_1 = 1$, $\gamma_2 = 0.3$, $\cos \theta_Y = -0.7$. The bending modulus c_b is 5×10^3 in both cases. To examine the deflection of the sheets, we plot the time history of the width $w(t)$ of the channel measured at its free end in figure 9. The sheets deflect inwards leading to a narrower opening at the free end in the wetting case, while the opposite is observed in the non-wetting case. The deflection is more significant in the

Moving contact lines on elastic sheets

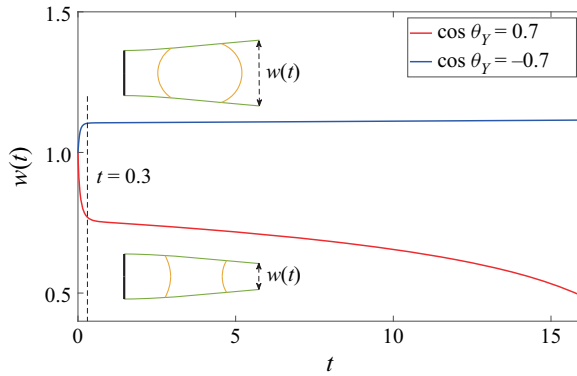


Figure 9. The channel width $w(t)$ at the free end versus time. The two curves correspond to the wetting case (lower) and non-wetting case (upper), respectively.

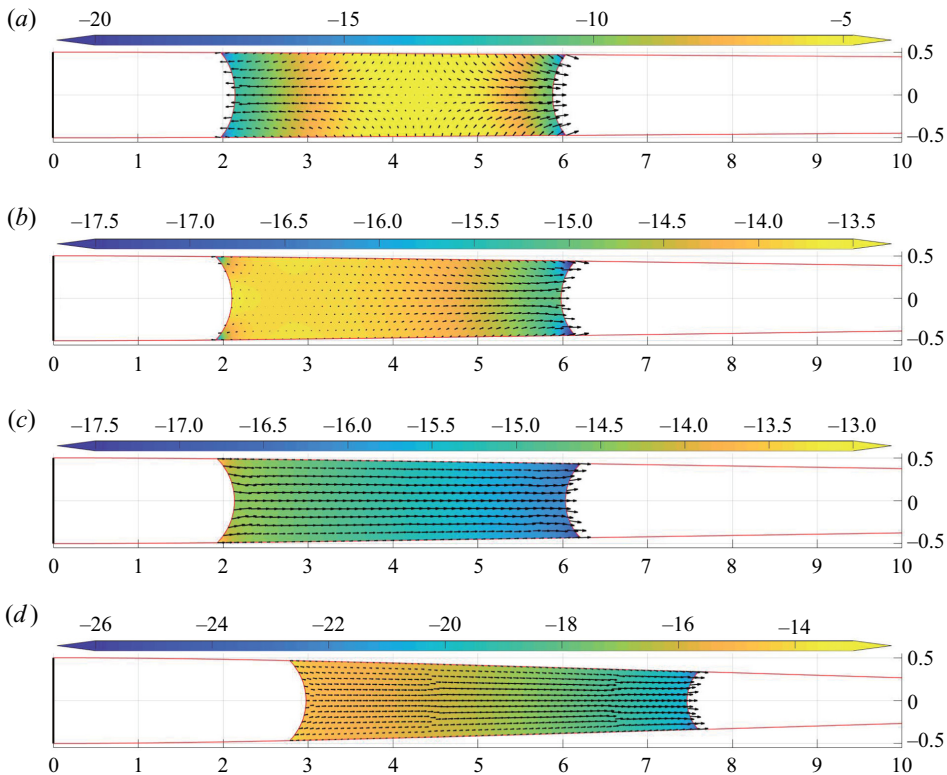


Figure 10. Snapshots of the wetting case ($\cos \theta_Y = 0.7$). The fluid velocity and pressure are shown using arrows and colour code, respectively: (a) $t = 0.05$; (b) $t = 0.3$; (c) $t = 1.0$; (d) $t = 15.0$.

wetting case. Furthermore, a rapid deflection of the sheets occurs at the beginning of the process ($t \lesssim 0.3$) in both cases. As shown in figures 10 and 11, the droplet remains nearly still in this stage. Droplet motion only occurs in the later stage ($t \gtrsim 0.3$) as a result of the sheet deflection.

The sheet deflection is mainly caused by the Laplace pressure of the droplet. In the wetting case, the pressure inside the droplet is negative (assuming zero pressure for the

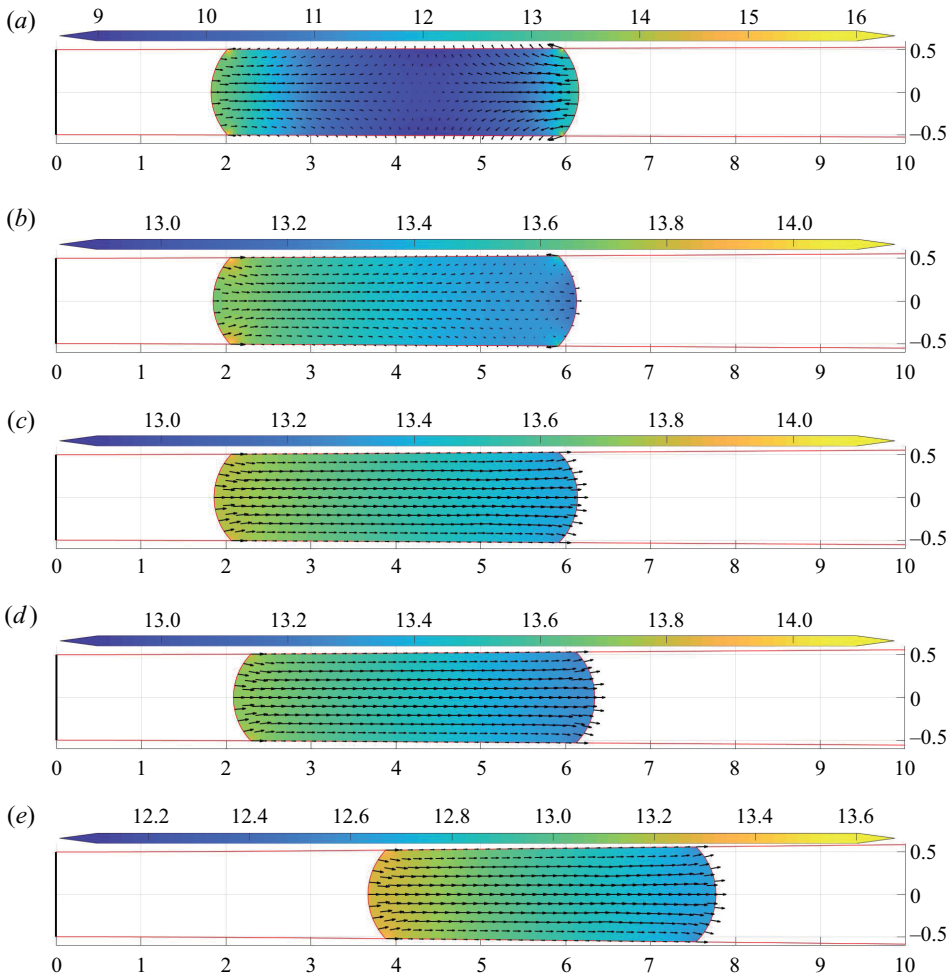


Figure 11. Snapshots of the non-wetting case ($\cos \theta_Y = -0.7$). The fluid velocity and pressure are shown using arrows and colour code, respectively: (a) $t = 0.05$; (b) $t = 0.3$; (c) $t = 1.0$; (d) $t = 15.0$; (e) $t = 90.0$.

vacuum), which causes the sheets to deflect inwards. In contrast, in the non-wetting case, the pressure of the droplet is positive, resulting in an outward sheet deflection. In addition, the capillary force at the contact line also contributes to the sheet deflection. The capillary force pulls the sheets inwards, which facilitates the inward deflection in the wetting case, but impedes the outward deflection in the non-wetting case. This explains the larger deflection in the wetting case as observed in [figure 9](#).

The deflection of the sheets results in a net force that drives the droplet towards the free end of the channel. Specifically, three forces mainly contribute to the droplet motion: (1) the bending force $\mathbf{f}_b = (c_b/Ca)(\Delta_s \kappa + \frac{1}{2} \kappa^3) \mathbf{n}$; (2) the sheet curvature force $\mathbf{f}_t = (1/Ca)(v - \gamma_1) \kappa \mathbf{n}$; and (3) the forces at the left and right contact lines $\mathbf{F}_{A_l, A_r} = (\gamma_3/Ca) \mathbf{m}_3$. For parameters used in the current simulation, we found that the force \mathbf{f}_t due to the sheet tension is negligible compared to the other two forces. In [figure 12](#), we show the horizontal component of the bending force at $t = 0.3$, $\mathbf{f}_b \cdot \mathbf{e}_1$, where $\mathbf{e}_1 = (1, 0)$. In both the wetting and non-wetting cases, the force has a rightward component, driving the droplet towards the free ends. The larger sheet deflection in the wetting case results in a

Moving contact lines on elastic sheets

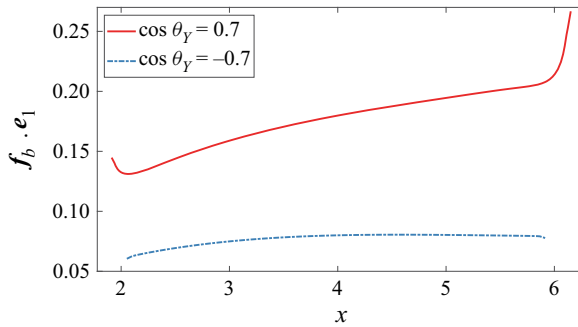


Figure 12. The horizontal component of the bending force, $f_b \cdot e_1$, along the sheet at $t = 0.3$. The two curves correspond to the wetting case (upper) and non-wetting case (lower), respectively.

larger bending force and consequently a faster droplet motion. The horizontal component of the contact line force, $(F_{\Lambda_1} + F_{\Lambda_2}) \cdot e_1$, equals 0.147 in the wetting case and -0.0763 in the non-wetting case at $t = 0.3$. The opposite sign is due to the opposite direction of the sheet deflection in the two cases. As a result, the rightward droplet motion is further enhanced by the contact line force in the wetting case but impeded in the non-wetting case.

To further examine the effects of wettability and stiffness of the sheets on the droplet dynamics, we carried out simulations with various contact angle θ_Y and bending modulus c_b . The numerical results are summarized in figure 13(a), where we plot the dynamics of the right (advancing) contact point x_r . After rescaling the time by

$$t \rightarrow A(\cos \theta_Y, c_b) \cdot t, \quad (5.3)$$

where A depends on $\cos \theta_Y$ and c_b , the data points for $(1/x_r(0) - 1/x_r(t))$ collapse into a master line with slope one. This shows that

$$x_r(t) = \frac{1}{\frac{1}{x_r(0)} - At}. \quad (5.4)$$

The deviation of data points from this master line is mainly due to the large deflection of the sheets; in fact, in the case of $\cos \theta_Y = 0.9$ and $c_b = 5000$, the free end of the channel is nearly closed when the droplet is close to that end, as shown in figure 13(d). Reducing the droplet size leads to smaller sheet deflection, in which case, a better agreement with the master line is observed (see the data points marked by ‘☆’).

The asymptotic relation (5.4) has been derived for small droplets under the lubrication approximation (Bradley *et al.* 2019). There, the fluid interface was assumed to have a circular profile, and the contact angle was equal to the equilibrium Young’s angle. It was shown that $A \propto |\cos \theta_Y|^2/c_b$. The dependence of A on θ_Y and c_b obtained from the current numerical results is shown in figure 13(b,c). While the inverse proportionality relation of A with the bending modulus c_b agrees with the asymptotic result, discrepancies are observed for the relation with $\cos \theta_Y$. First of all, we find that A is asymmetric about $\cos \theta_Y$. With the same value of $|\cos \theta_Y|$, A is larger in the wetting case than in the non-wetting case. A larger value of A corresponds to a faster droplet motion. Second, we observe that $A \propto |\cos \theta_Y|^\alpha$, where α is slightly less than 2 in the wetting case but larger than 2 in the non-wetting case. We believe that these discrepancies are mainly due to the contribution of the capillary force at the contact line, which was not fully taken into account in the previous asymptotic results. The capillary force of wetting droplets induces larger sheet

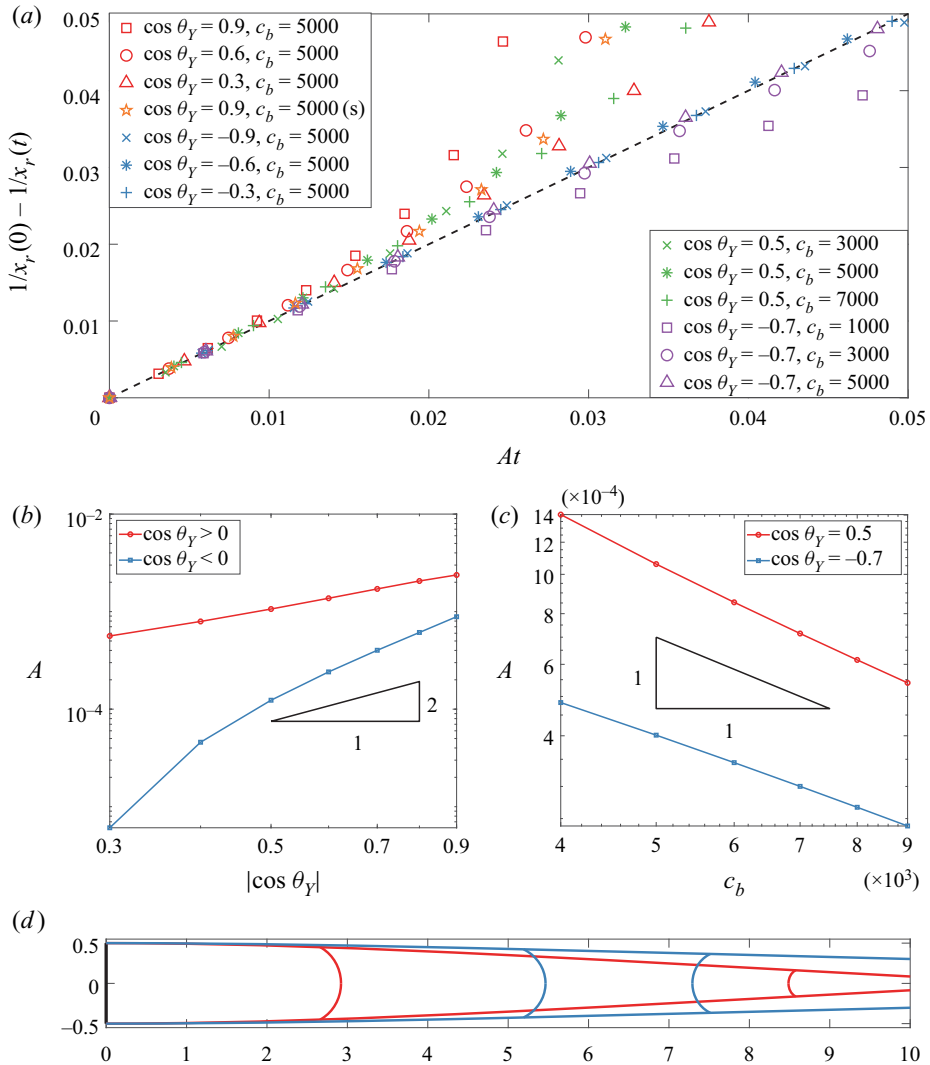


Figure 13. (a) The dynamics of a droplet driven by bendotaxis with different contact angle θ_Y and different bending modulus c_b . The data points marked by ‘ \star ’ are for a smaller droplet, whose size is one half that of the droplet in all other simulations. The dashed line has slope 1. (b) Doubly logarithmic plot of the coefficient A versus $|\cos \theta_Y|$, where $c_b = 5000$. (c) Doubly logarithmic plot of coefficient A versus c_b . (d) Configurations of the two systems with $\cos \theta_Y = 0.9$ and $c_b = 5000$ (marked by ‘ \square ’ and ‘ \star ’ in panel a) at $At = 0.024$. The droplet in blue is half the size of that one in red.

deflections and consequently faster droplet motions. In addition, the finite droplet size also contributes to the discrepancies.

6. Conclusion

In this work, we considered the dynamics of a moving contact line on an elastic sheet. Based on generalized thermodynamics, we derived a hydrodynamic model, in particular, the necessary boundary conditions on the sheet and at the moving contact line. These boundary conditions can be interpreted as the balance of various forces. They were

obtained by analysing the different energy dissipation mechanisms, in which the relevant fluxes and their corresponding forces were identified. The resulting model obeys an energy law, where the total energy of the dynamical system dissipates via the viscous force in the bulk fluids and the friction forces on the fluid–sheet interface and at the moving contact line.

The boundary conditions are summarized as follows. In the tangential direction of the sheet, the boundary conditions are given by the balance of the fluid shear stress with the friction force and the gradient of the sheet tension, respectively. The friction force is due to the slip between the fluids and the sheet. In the normal direction of the sheet, the boundary condition is given by the balance of the fluid normal stress with the bending force and the curvature force of the sheet. At the moving contact line, in the tangential direction to the sheet, the Young stress of the fluid interface is balanced by the friction force and the jump of the sheet tension, respectively. Here the Young stress refers to the capillary force arising from the deviation of the dynamic contact angle from the equilibrium angle, and the friction force is due to the motion of the contact line relative to the sheet. In the normal direction to the sheet, the capillary force of the fluid interface balances with the jump of the gradient of the sheet curvature. These force balances, together with the kinematic and inextensibility conditions, form the complete boundary conditions on the sheet for the hydrodynamic model.

Using this model, we numerically studied the relaxation dynamic of droplets on elastic sheets and the droplet motion driven by bendotaxis in a channel bounded by elastic sheets. In both applications, the full hydrodynamic model provided detailed information on the respective physical process. In addition to the usual hydrodynamic quantities such as the fluid velocity field and pressure, the interface and sheet profiles, we also obtained the dynamic contact angle, the slip velocity, the tension of the sheet, etc. This allowed us to better understand the dynamical processes as compared to simplified models (e.g. thin-film models).

For the relaxation dynamics of droplets on elastic sheets, we simulated two types of systems, one in the wetting case and the other in the non-wetting case. The numerical results verified the energy decay property of the model. The profiles of the fluid interface and the sheet at the steady state agreed well with the asymptotic solutions derived in an earlier work (Zhang *et al.* 2020).

For the motion of a droplet driven by bendotaxis, we simulated the dynamical process and investigated the mechanism of the droplet motion. We identified two stages in the dynamical process, one being an initial period in which the sheets were deflected, and the other being the subsequent period in which droplet transport occurred. We found that the sheet deflection was caused by the Laplace pressure of the droplet and the capillary force of the fluid interface. The latter always pulled the sheets inwards, thus it enhanced the inward deflection in the wetting case but hindered the outward deflection in the non-wetting case. A larger sheet deflection resulted in larger bending forces and consequently a faster droplet motion. Our numerical results also showed that the motion of a wetting (respectively non-wetting) droplet was further enhanced (respectively hindered) by the combined contact line forces. Furthermore, we examined the effect of the droplet wettability and sheet stiffness on the dynamics. After a proper rescaling of time, the dynamics of the various systems collapsed into a universal line.

The two applications demonstrate that our model is able to model complex fluid–sheet interactions in the presence of moving contact lines. With this model, we are in a position to systematically study many interesting elastocapillary problems, such as capillary rise in elastic tubes, spontaneous wrapping of liquid drops by elastic sheets, bubble dynamics

on porous polymer films, etc. The model can be generalized to three dimensions in a straightforward manner, where the boundary and contact line conditions will take similar forms as in two dimensions. Simulations for 3-D problems become more challenging in view of the requirements for quality mesh generation and efficient solvers. We will leave these problems to the future work.

Acknowledgments. We thank an anonymous reviewer for helpful discussions on the arguments leading to the force balance equations (3.15), (3.16) and (3.21).

Funding. The work of W.R. was supported in part by Singapore MOE Academic Research Fund Tier 2 (Project No. MOE-T2EP20120-0009) and NSFC (No. 11871365). The work of Z.Z. was partially supported by the NSFC grant (No. 11731006, No. 12071207), NSFC Tianyuan-Pazhou grant (No. 12126602), the Guangdong Basic and Applied Basic Research Foundation (2021A1515010359), and the Guangdong Provincial Key Laboratory of Computational Science and Material Design (No. 2019B030301001).

Declaration of interests. The authors report no conflict of interest.

Author ORCID.

 Weiqing Ren <https://orcid.org/0000-0001-5730-867X>.

Appendix A. Variation of the Willmore energy

We provide some results from differential geometry that were used to compute the variation of the energies in § 3. Let $\mathbf{q}(\xi, t) = (x(\xi, t), y(\xi, t))$ denote a curve Γ parametrized by $\xi \in D_\xi$. The tangent, normal and curvature of the curve are respectively given by

$$\left. \begin{aligned} \boldsymbol{\tau} &= \frac{1}{|\partial_\xi \mathbf{q}|} \left(\frac{\partial x}{\partial \xi}, \frac{\partial y}{\partial \xi} \right), \\ \mathbf{n} &= \frac{1}{|\partial_\xi \mathbf{q}|} \left(\frac{\partial y}{\partial \xi}, -\frac{\partial x}{\partial \xi} \right), \\ \kappa &= \nabla_s \cdot \mathbf{n} = \frac{1}{|\partial_\xi \mathbf{q}|^3} \left(\frac{\partial x}{\partial \xi} \frac{\partial^2 y}{\partial \xi^2} - \frac{\partial y}{\partial \xi} \frac{\partial^2 x}{\partial \xi^2} \right). \end{aligned} \right\} \quad (\text{A1})$$

In addition, we have $\partial_\xi \boldsymbol{\tau} = -|\partial_\xi \mathbf{q}| \kappa \mathbf{n}$ and $\partial_\xi \mathbf{n} = |\partial_\xi \mathbf{q}| \kappa \boldsymbol{\tau}$.

Let \mathcal{D} be a differential operator. We have

$$\mathcal{D}|\partial_\xi \mathbf{q}| = \frac{1}{|\partial_\xi \mathbf{q}|} \frac{\partial \mathbf{q}}{\partial \xi} \cdot \frac{\partial \mathcal{D} \mathbf{q}}{\partial \xi} = (\nabla_s \cdot \mathcal{D} \mathbf{q}) |\partial_\xi \mathbf{q}|, \quad (\text{A2})$$

where $\nabla_s = (1/|\partial_\xi \mathbf{q}|^2)(\partial \mathbf{q}/\partial \xi)(\partial/\partial \xi)$ is the surface gradient. For a given function f defined on the curve Γ , we have

$$\frac{d}{dt} \int_\Gamma f(\mathbf{q}, t) ds = \int_\Gamma \left(\frac{\partial f}{\partial t} + \dot{\mathbf{q}} \cdot \nabla f + (\nabla_s \cdot \dot{\mathbf{q}}) f \right) ds, \quad (\text{A3})$$

where we have used (A2) with $\mathcal{D} = \partial/\partial t$.

The surface divergence theorem for a vector function $F(\xi)$ defined on Γ reads

$$\begin{aligned} \int_{\Gamma} \nabla_s \cdot F \, ds &= \int_{D_\xi} \boldsymbol{\tau} \cdot \partial_\xi F \, d\xi \\ &= (F \cdot \mathbf{m}) \Big|_{\partial\Gamma} - \int_{D_\xi} F \cdot \partial_\xi \boldsymbol{\tau} \, d\xi \\ &= (F \cdot \mathbf{m}) \Big|_{\partial\Gamma} + \int_{\Gamma} \kappa F \cdot \mathbf{n} \, ds, \end{aligned} \tag{A4}$$

where \mathbf{m} is the outward conormal of Γ .

Applying the differential operator \mathcal{D} on the curvature κ , we obtain

$$\begin{aligned} \mathcal{D}\kappa &= \mathcal{D}(\nabla_s \cdot \mathbf{n}) = \mathcal{D} \left(\frac{\boldsymbol{\tau}}{|\partial_\xi \mathbf{q}|} \cdot \partial_\xi \mathbf{n} \right) \\ &= \frac{\mathcal{D}\boldsymbol{\tau}}{|\partial_\xi \mathbf{q}|} \cdot \partial_\xi \mathbf{n} + \mathcal{D} \left(\frac{1}{|\partial_\xi \mathbf{q}|} \right) \boldsymbol{\tau} \cdot \partial_\xi \mathbf{n} + \frac{\boldsymbol{\tau}}{|\partial_\xi \mathbf{q}|} \cdot \frac{\partial}{\partial \xi} (\mathcal{D}\mathbf{n}) \\ &= \left[-(\nabla_s \cdot (\mathcal{D}\mathbf{q}))(\nabla_s \cdot \mathbf{n}) + \frac{1}{|\partial_\xi \mathbf{q}|^2} \frac{\partial}{\partial \xi} (\mathcal{D}\mathbf{q}) \cdot \partial_\xi \mathbf{n} \right] - \nabla_s \cdot (\mathcal{D}\mathbf{q}) \frac{\boldsymbol{\tau}}{|\partial_\xi \mathbf{q}|} \cdot \partial_\xi \mathbf{n} \\ &\quad + \nabla_s \cdot \left[-\nabla_s (\mathcal{D}\mathbf{q} \cdot \mathbf{n}) + \frac{\boldsymbol{\tau}}{|\partial_\xi \mathbf{q}|} (\mathcal{D}\mathbf{q} \cdot \partial_\xi \mathbf{n}) \right] \\ &= -\Delta_s (\mathcal{D}\mathbf{q} \cdot \mathbf{n}) - \kappa (\nabla_s \cdot (\mathcal{D}\mathbf{q})) + \nabla_s \cdot [\boldsymbol{\tau} (\kappa \boldsymbol{\tau} \cdot (\mathcal{D}\mathbf{q}))] \\ &= -\Delta_s (\mathcal{D}\mathbf{q} \cdot \mathbf{n}) - (\mathcal{D}\mathbf{q} \cdot \mathbf{n}) \kappa^2 + \nabla_s \kappa \cdot (\mathcal{D}\mathbf{q}), \end{aligned} \tag{A5}$$

where we have used $\partial_\xi \boldsymbol{\tau} = -|\partial_\xi \mathbf{q}| \kappa \mathbf{n}$ in the last step.

Finally, the time derivative of the Willmore energy of Γ is given by

$$\begin{aligned} \frac{d}{dt} \int_{\Gamma} \kappa^2 \, ds &= \int_{\Gamma} \left(2\kappa \frac{\partial}{\partial t} \kappa + \kappa^2 (\nabla_s \cdot \dot{\mathbf{q}}) \right) ds \\ &= \int_{\Gamma} -2\kappa \Delta_s (\dot{\mathbf{q}} \cdot \mathbf{n}) - 2(\dot{\mathbf{q}} \cdot \mathbf{n}) \kappa^3 + \nabla_s \cdot (\kappa^2 \dot{\mathbf{q}}) \, ds \\ &= 2 \int_{\Gamma} (-\dot{\mathbf{q}} \cdot \mathbf{n}) \left(\Delta_s \kappa + \frac{1}{2} \kappa^3 \right) ds \\ &\quad + 2 \left(-\kappa \mathbf{m} \cdot \nabla_s (\dot{\mathbf{q}} \cdot \mathbf{n}) + (\mathbf{m} \cdot \nabla_s \kappa) (\dot{\mathbf{q}} \cdot \mathbf{n}) + \frac{1}{2} \kappa^2 \dot{\mathbf{q}} \cdot \mathbf{m} \right) \Big|_{\partial\Gamma}, \end{aligned} \tag{A6}$$

where we have used (A3) with $f = \kappa^2$ in the first step, (A5) with $\mathcal{D} = \partial/\partial t$ in the second step, and the divergence theorem (A4) as well as integration by parts in the last step.

Appendix B. Weak formulation of the model

In this appendix, we give the weak formulation of the model that was used to simulate the drop relaxation dynamics in § 4. We parametrize the fluid interface as $\mathbf{r}(\zeta)$ where $\zeta \in [0, 1]$ and the sheet as $\mathbf{q}(x) = (x, y(x))$ where $x \in [-1, 1]$. The two contact lines of the droplet are located at $\mathbf{r}(0) = (x_l, y(x_l))$ and $\mathbf{r}(1) = (x_r, y(x_r))$.

We define the following respective function spaces for the fluid velocity, the fluid pressure and the sheet tension,

$$\mathbb{U} = \{\boldsymbol{\omega} \in [H^1(\Omega)]^2, \boldsymbol{\omega} = \mathbf{0} \text{ on } \Sigma_3\}, \tag{B1}$$

$$\mathbb{P} = \left\{ \varphi \in L^2(\Omega), \int_{\Omega} \varphi \, dx = 0 \right\}, \tag{B2}$$

$$V_1 = H^1([x_l, x_r]), \quad V_2 = \{g \in H^1([-1, x_l] \cup [x_r, 1]), g(-1) = g(1) = 0\}. \tag{B3}$$

We take the inner product of (3.26a) with $\boldsymbol{\omega} \in \mathbb{U}$, (3.26b) with $\varphi \in \mathbb{P}$, (3.35) with $f \in H^1([-1, 1])$, (3.32) with $g_1 \in V_1$ and $g_2 \in V_2$, and (3.27c) with $\boldsymbol{\psi} \in H^1([0, 1]) \times H_0^1([0, 1])$. Furthermore, we take the inner product of $\kappa/|\partial_x \mathbf{q}| = \Delta_s y$ with $\beta \in H_0^1([-1, 1])$. Using the interface and boundary conditions, we obtain the following equations:

$$-(p, \nabla \cdot \boldsymbol{\omega})_{\Omega} + (\eta(\nabla \mathbf{u} + (\nabla \mathbf{u})^T), \nabla \boldsymbol{\omega})_{\Omega} + \frac{1}{Ca} (\partial_s r, \partial_s \boldsymbol{\omega})_{\Sigma_3} \tag{B4a}$$

$$-\frac{1}{Ca} (v, \nabla_s \cdot \boldsymbol{\omega})_{\mathcal{E}} + \frac{1}{Ca} \left(c_b \partial_s \left(\frac{\kappa}{|\partial_x \mathbf{q}|} \right) + \frac{3c_b}{2} \kappa^2 \partial_s y - \gamma \partial_s y, \partial_s (|\partial_x \mathbf{q}| \boldsymbol{\omega} \cdot \mathbf{n}) \right)_{\mathcal{E}}$$

$$+ \frac{\gamma_1 - \gamma_2}{Ca} ((|\partial_x \mathbf{q}| \omega_1)|_{\Lambda_r} - (|\partial_x \mathbf{q}| \omega_1)|_{\Lambda_l}) = 0, \quad \forall \boldsymbol{\omega} = (\omega_1, \omega_2) \in \mathbb{U},$$

$$(\nabla \cdot \mathbf{u}, \varphi)_{\Omega} = 0, \quad \forall \varphi \in \mathbb{P}, \tag{B4b}$$

$$\left(\frac{\partial y}{\partial t}, f \right)_{\mathcal{E}} + (|\partial_x \mathbf{q}| \mathbf{u} \cdot \mathbf{n}, f)_{\mathcal{E}} = 0, \quad \forall f \in H^1([-1, 1]), \tag{B4c}$$

$$\frac{l_s}{\mu_1} (\partial_s v, \partial_s g_1)_{\Sigma_1} + Ca (\nabla_s \cdot \mathbf{u}, g_1)_{\Sigma_1} + \frac{1}{\mu_{\Lambda}} (\llbracket v \rrbracket_2^1 g_1) \Big|_{\Lambda} = 0, \quad \forall g_1 \in V_1, \tag{B4d}$$

$$\frac{l_s}{\mu_2} (\partial_s v, \partial_s g_2)_{\Sigma_2} + Ca (\nabla_s \cdot \mathbf{u}, g_2)_{\Sigma_2} - \frac{1}{\mu_{\Lambda}} (\llbracket v \rrbracket_2^1 g_2) \Big|_{\Lambda} = 0, \quad \forall g_2 \in V_2, \tag{B4e}$$

$$(\dot{\mathbf{r}}, \boldsymbol{\psi})_{\Sigma_3} - (\mathbf{u}, \boldsymbol{\psi})_{\Sigma_3} = 0, \quad \forall \boldsymbol{\psi} \in H^1([0, 1]) \times H_0^1([0, 1]), \tag{B4f}$$

$$\left(\frac{\kappa}{|\partial_x \mathbf{q}|}, \beta \right)_{\mathcal{E}} + (\partial_s y, \partial_s \beta)_{\mathcal{E}} = 0, \quad \forall \beta \in H_0^1([-1, 1]), \tag{B4g}$$

where $w|_{\Lambda_l}$ and $w|_{\Lambda_r}$ denote the value of w at the left and right contact lines, respectively; η takes the value η_1 in Ω_1 and η_2 in Ω_2 ; and γ takes the value γ_1 on Σ_1 and γ_2 on Σ_2 . The operator ∂_s represents $(1/|\partial_x \mathbf{q}|)(\partial/\partial x)$ on the sheet and $(1/|\partial_{\zeta} \mathbf{r}|)(\partial/\partial \zeta)$ on the fluid–fluid interface. The inner products in the above equations are defined as

$$(\mathbf{u}, \mathbf{v})_{\Omega} = \sum_{i=1}^2 \int_{\Omega_i(t)} \mathbf{u} \cdot \mathbf{v} \, dx, \tag{B5a}$$

$$(u, v)_{\Sigma_1} = \int_{x_l}^{x_r} u(x)v(x)|\partial_x \mathbf{q}| \, dx, \tag{B5b}$$

$$(u, v)_{\Sigma_2} = \int_{-1}^{x_l} u(x)v(x)|\partial_x \mathbf{q}| \, dx + \int_{x_r}^1 u(x)v(x)|\partial_x \mathbf{q}| \, dx, \tag{B5c}$$

Moving contact lines on elastic sheets

$$(u, v)_{\Sigma} = (u, v)_{\Sigma_1} + (u, v)_{\Sigma_2}, \quad (\text{B5d})$$

$$(u, v)_{\Sigma_3} = \int_0^1 \mathbf{u}(\zeta) \cdot \mathbf{v}(\zeta) |\partial_{\zeta} \mathbf{r}| d\zeta. \quad (\text{B5e})$$

REFERENCES

- ALBEN, S., GORODETSKY, A.A., KIM, D. & DEEGAN, R.D. 2019 Semi-implicit methods for the dynamics of elastic sheets. *J. Comput. Phys.* **399**, 108952.
- ANDREOTTI, B. & SNOEIJER, J.H. 2020 Statics and dynamics of soft wetting. *Annu. Rev. Fluid Mech.* **52**, 285–308.
- ANTKOWIAK, A., AUDOLY, B., JOSSEAND, C., NEUKIRCH, S. & RIVETTI, M. 2011 Instant fabrication and selection of folded structures using drop impact. *Proc. Natl Acad. Sci.* **108** (26), 10400–10404.
- BARDALL, A., DANIELS, K.E. & SHEARER, M. 2018 Deformation of an elastic substrate due to a resting sessile droplet. *Eur. J. Appl. Maths* **29** (2), 281–300.
- BARRETT, J.W., GARCKE, H. & NÜRNBERG, R. 2017 Finite element approximation for the dynamics of fluidic two-phase biomembranes. *ESAIM: Math. Model. Numer. Anal.* **51** (6), 2319–2366.
- BARRETT, J.W., GARCKE, H. & NÜRNBERG, R. 2020 Parametric finite element approximations of curvature-driven interface evolutions. In *Handbook of Numerical Analysis* (ed. A. Bonito & R.H. Nochetto), vol. 21, pp. 275–423. Elsevier.
- BICO, J., REYSSAT, É. & ROMAN, B. 2018 Elastocapillarity: when surface tension deforms elastic solids. *Annu. Rev. Fluid Mech.* **50**, 629–659.
- BRADLEY, A.T., BOX, F., HEWITT, I.J. & VELLA, D. 2019 Wettability-independent droplet transport by bendotaxis. *Phys. Rev. Lett.* **122** (7), 074503.
- BRADLEY, A.T., HEWITT, I.J. & VELLA, D. 2021 Droplet trapping in bendotaxis caused by contact angle hysteresis. *Phys. Rev. Fluids* **6** (11), 114003.
- BRUBAKER, N.D. 2019 Two-dimensional capillary origami with inextensibility and free triple-contact points. *SIAM J. Appl. Maths* **79** (2), 572–593.
- BRUBAKER, N.D. & LEGA, J. 2016 Capillary-induced deformations of a thin elastic sheet. *Phil. Trans. R. Soc. A* **374**, 20150169.
- CARRÉ, A., GASTEL, J.-C. & SHANAHAN, M.E.R. 1996 Viscoelastic effects in the spreading of liquids. *Nature* **379**, 432–434.
- CHEN, C. & ZHANG, T. 2022 Coupling lattice model and many-body dissipative particle dynamics to make elastocapillary simulation simple. *Extreme Mech. Lett.* **54**, 101741.
- DAS, S., MARCHAND, A., ANDREOTTI, B. & SNOEIJER, J.H. 2011 Elastic deformation due to tangential capillary forces. *Phys. Fluids* **23** (7), 072006.
- DAVIDOVITCH, B. & VELLA, D. 2018 Partial wetting of thin solid sheets under tension. *Soft Matt.* **14** (24), 4913–4934.
- DUPRAT, C., ARISTOFF, J.M. & STONE, H.A. 2011 Dynamics of elastocapillary rise. *J. Fluid Mech.* **679**, 641–654.
- EXTRAND, C.W. & KUMAGAI, Y. 1996 Contact angles and hysteresis on soft surfaces. *J. Colloid Interface Sci.* **184** (1), 191–200.
- FARUTIN, A. & MISBAH, C. 2014 Symmetry breaking and cross-streamline migration of three-dimensional vesicles in an axial Poiseuille flow. *Phys. Rev. E* **89** (4), 042709.
- HELFRICH, W. 1973 Elastic properties of lipid bilayers: theory and possible experiments. *Z. Naturforsch. C* **28** (11), 693–703.
- HOWLAND, C.J., ANTKOWIAK, A., CASTREJÓN-PITA, J.R., HOWISON, S.D., OLIVER, J.M., STYLE, R.W. & CASTREJÓN-PITA, A.A. 2016 It's harder to splash on soft solids. *Phys. Rev. Lett.* **117** (18), 184502.
- HUANG, J., JUSZKIEWICZ, M., DE JEU, W.H., CERDA, E., EMRICK, T., MENON, N. & RUSSELL, T.P. 2007 Capillary wrinkling of floating thin polymer films. *Science* **317** (5838), 650–653.
- HUI, C.-Y. & JAGOTA, A. 2014 Deformation near a liquid contact line on an elastic substrate. *Proc. R. Soc. A* **470** (2167), 20140085.
- JERISON, E.R., XU, Y., WILEN, L.A. & DUFRESNE, E.R. 2011 Deformation of an elastic substrate by a three-phase contact line. *Phys. Rev. Lett.* **106** (18), 186103.
- KAJIYA, T., DAERR, A., NARITA, T., ROYON, L., LEQUEUX, F. & LIMAT, L. 2013 Advancing liquid contact line on visco-elastic gel substrates: stick-slip vs. continuous motions. *Soft Matt.* **9** (2), 454–461.
- KARPITSCHKA, S., DAS, S., VAN GORCUM, M., PERRIN, H., ANDREOTTI, B. & SNOEIJER, J.H. 2015 Droplets move over viscoelastic substrates by surfing a ridge. *Nat. Commun.* **6**, 7891.

- KIM, H.-Y. & MAHADEVAN, L. 2006 Capillary rise between elastic sheets. *J. Fluid Mech.* **548**, 141–150.
- KUSUMAATMAJA, H., LI, Y., DIMOVA, R. & LIPOWSKY, R. 2009 Intrinsic contact angle of aqueous phases at membranes and vesicles. *Phys. Rev. Lett.* **103** (23), 238103.
- KUSUMAATMAJA, H. & LIPOWSKY, R. 2011 Droplet-induced budding transitions of membranes. *Soft Matt.* **7** (15), 6914–6919.
- LIMAT, L. 2012 Straight contact lines on a soft, incompressible solid. *Eur. Phys. J. E* **35**, 134.
- LUO, Z.Y. & BAI, B.F. 2015 Dynamics of biconcave vesicles in a confined shear flow. *Chem. Engng Sci.* **137**, 548–555.
- NEUKIRCH, S., ANTKOWIAK, A. & MARIGO, J.-J. 2013 The bending of an elastic beam by a liquid drop: a variational approach. *Proc. R. Soc. A* **469** (2157), 20130066.
- OLIVES, J. 1993 Capillarity and elasticity. The example of the thin plate. *J. Phys.: Condens. Matter* **5**, 2081–2094.
- OLIVES, J. 1996 A combined capillarity and elasticity problem for a thin plate. *SIAM J. Appl. Maths* **56** (2), 480–493.
- PAULSEN, J.D., DÉMERY, V., SANTANGELO, C.D., RUSSELL, T.P., DAVIDOVITCH, B. & MENON, N. 2015 Optimal wrapping of liquid droplets with ultrathin sheets. *Nat. Mater.* **14** (12), 1206–1209.
- PEPONA, M., SHEK, A.C.M., SEMPREBON, C., KRÜGER, T. & KUSUMAATMAJA, H. 2021 Modeling ternary fluids in contact with elastic membranes. *Phys. Rev. E* **103** (2–1), 022112.
- PÉRAUD, J.-P. & LAUGA, E. 2014 Geometry and wetting of capillary folding. *Phys. Rev. E* **89** (4), 043011.
- PERICET-CÁMARA, R., BEST, A., BUTT, H.-J. & BONACCURSO, E. 2008 Effect of capillary pressure and surface tension on the deformation of elastic surfaces by sessile liquid microdrops: an experimental investigation. *Langmuir* **24** (19), 10565–10568.
- POZRIKIDIS, C. & HILL, A.I. 2014 Deformation of an elastic substrate due to a sessile drop. *Eur. J. Mech. B/Fluids* **43**, 90–99.
- PY, C., REVERDY, P., DOPPLER, L., BICO, J., ROMAN, B. & BAROUD, C.N. 2007 Capillary origami: spontaneous wrapping of a droplet with an elastic sheet. *Phys. Rev. Lett.* **98** (15), 156103.
- PY, C., REVERDY, P., DOPPLER, L., BICO, J., ROMAN, B. & BAROUD, C.N. 2009 Capillarity induced folding of elastic sheets. *Eur. Phys. J. Spec. Top.* **166**, 67–71.
- REN, W., HU, D. & WEINAN, W. 2010 Continuum models for the contact line problem. *Phys. Fluids* **22** (10), 102103.
- REN, W. & WEINAN, W. 2011 Derivation of continuum models for the moving contact line problem based on thermodynamic principles. *Commun. Math. Sci.* **9** (2), 597–606.
- SCHROLL, R.D., ADDA-BEDIA, M., CERDA, E., HUANG, J., MENON, N., RUSSELL, T.P., TOGA, K.B., VELLA, D. & DAVIDOVITCH, B. 2013 Capillary deformations of bendable films. *Phys. Rev. Lett.* **111** (1), 014301.
- SHANAHAN, M.E.R. 1985 Contact angle equilibrium on thin elastic solids. *J. Adhes.* **18** (4), 247–267.
- SHANAHAN, M.E.R. 1987a Equilibrium of liquid drops on thin plates; plate rigidity and stability considerations. *J. Adhes.* **20** (4), 261–274.
- SHANAHAN, M.E.R. 1987b The influence of solid micro-deformation on contact angle equilibrium. *J. Phys. D: Appl. Phys.* **20** (7), 945.
- SHANAHAN, M.E.R. 1988 The spreading dynamics of a liquid drop on a viscoelastic solid. *J. Phys. D: Appl. Phys.* **21** (6), 981.
- STYLE, R.W., BOLTYANSKIY, R., CHE, Y., WETTLAUFER, J.S., WILEN, L.A. & DUFRESNE, E.R. 2013 Universal deformation of soft substrates near a contact line and the direct measurement of solid surface stresses. *Phys. Rev. Lett.* **110** (6), 066103.
- STYLE, R.W. & DUFRESNE, E.R. 2012 Static wetting on deformable substrates, from liquids to soft solids. *Soft Matt.* **8** (27), 7177–7184.
- STYLE, R.W., JAGOTA, A., HUI, C.-Y. & DUFRESNE, E.R. 2017 Elastocapillarity: surface tension and the mechanics of soft solids. *Annu. Rev. Condens. Matter Phys.* **8**, 99–118.
- TARONI, M. & VELLA, D. 2012 Multiple equilibria in a simple elastocapillary system. *J. Fluid Mech.* **712**, 273–294.
- VELLA, D., ADDA-BEDIA, M. & CERDA, E. 2010 Capillary wrinkling of elastic membranes. *Soft Matt.* **6** (22), 5778–5782.
- WOUTERS, M., AOUANE, O., KRÜGER, T. & HARTING, J. 2019 Mesoscale simulation of soft particles with tunable contact angle in multicomponent fluids. *Phys. Rev. E* **100** (3–1), 033309.
- YAZDANI, A. & BAGCHI, P. 2012 Three-dimensional numerical simulation of vesicle dynamics using a front-tracking method. *Phys. Rev. E* **85** (5), 056308.
- ZHANG, Z. & QIAN, T. 2022 Variational approach to droplet transport via bendotaxis: thin film dynamics and model reduction. *Phys. Rev. Fluids* **7** (4), 044002.

Moving contact lines on elastic sheets

- ZHANG, Z., YAO, J. & REN, W. 2020 Static interface profiles for contact lines on an elastic membrane with the willmore energy. *Phys. Rev. E* **102** (6), 062803.
- ZHAO, Q., REN, W. & ZHANG, Z. 2021 A thermodynamically consistent model and its conservative numerical approximation for moving contact lines with soluble surfactants. *Comput. Meth. Appl. Mech. Engng* **385**, 114033.
- ZHAO, H. & SHAQFEH, E.S.G. 2013 The shape stability of a lipid vesicle in a uniaxial extensional flow. *J. Fluid Mech.* **719**, 345–361.
- ZHAO, H., SPANN, A.P. & SHAQFEH, E.S.G. 2011 The dynamics of a vesicle in a wall-bound shear flow. *Phys. Fluids* **23** (12), 121901.